Hindawi
Adsorption Science & Technology
Volume 2021, Article ID 9732092, 24 pages
https://doi.org/10.1155/2021/9732092

Research Article

How the Solid/Liquid Ratio Affects the Cation Exchange Process and Porosity in the Case of Dioctahedral Smectite: Structural Analysis?

Chadha Mejri, Walid Oueslati, and Abdesslem Ben Haj Amara

Université de Carthage, Faculté des Sciences de Bizerte, LR19ES20: Ressources, Matériaux et Ecosystèmes (RME), 7021 Bizerte, Tunisia

Correspondence should be addressed to Walid Oueslati; walidoueslati@ymail.com

Received 11 May 2021; Revised 22 July 2021; Accepted 11 September 2021; Published 14 October 2021

Academic Editor: Hai-Bo Qin

The performance of a clay mineral geomembrane used in the context of a geological barrier for industrial and radioactive waste confinement must pass through the understanding of its hydrous response as well as the limits of the cation exchange process which are closely related to the solid/liquid ratio constraint. The Na-rich montmorillonite is used, as starting material, to evaluate the link between the applied external constraint (variable solid/liquid ratio) and the structural response of the material. The geochemical constraint is realized at the laboratory scale, and the possible effects are investigated in the cases of Ba^{2+} and Ni^{2+} heavy metal cations. The structural analysis is achieved using the XRD profile modeling approach to quantify the interlayer space (IS) deformation. The quantitative XRD analysis, which consists of the comparison of experimental 001 reflections with the calculated ones deduced from structural models, allowed us to determine the optimal structural parameters describing IS configuration along the $c*$ axis. The obtained result showed an interstratified hydration character, for both studied exchangeable cations, regardless of the solid/liquid ratio being described probably by a partial cation exchange process. The theoretical mixed layer structure (MLS) suggests the coexistence of more one cristallite species saturated by more than one exchangeable cations, indicating a partial saturation of all exchangeable sites. The optimum structural parameter values, from the theoretical model, allowed us to follow the evolution of several intrinsic properties versus the applied constraint strength. The variable solid/liquid ratio effect on the material porosity is examined by the BET-specific surface area and BJH pore size distribution (PSD) analyses. The adsorption measurement outcomes confirm XRD results concerning mainly the link between several intrinsic clay properties and the constraint strength.

1. Introduction

Clays are considered among the best candidates as a depolluting agent, specifically montmorillonite (2 : 1 phyllosilicate groups), which belongs to the smectite family [1–4]. In addition to their great use in the pharmaceutical and cosmetic fields, smectite is used in the concept of the natural geological barrier for industrial and radioactive waste confinement [5–10]. The phyllosilicate structure specificity (layered structure, cation exchange capacity (CEC), permeability, hydration characteristics, specific surface area (SSA), porosity, mechanical resistance, great availability in nature, low-cost materials…) makes it possible to achieve these objectives [11–13]. Also, montmorillonite, attapulgite, zeolite, kaolinite, sepiolite, vermiculite, and illite are used for remediation and fixing heavy metal pollution in soil. Several works [14–16] confirmed that clay minerals are one of the main components of heavy metal adsorption and passivation in soil. Several determining factors make clay a strong candidate in the context of heavy metal adsorption. Indeed, [17–19] demonstrate that the adsorption capability is mainly affected by the CEC and the SSA values. Also, [20] shows that the contact time (CT) influences the heavy metal adsorption rate of clay mineral. For laboratory experiments, a satisfactory amount of heavy metals can be adsorbed within the first 3 h, and in some cases, a total adsorption was achieved in

6 h depending on other factors such as clay mineral composition, heavy metal cation type, and pH of the system [21, 22]. Many authors [21–26] demonstrate the important role played by the pH of the system in the adsorption of heavy metals by the clay mineral process as it affects the leachability of heavy metal cations. There is a linearly proportional relationship between the pH rate fluctuation and the rate of adsorption. The clay dosage is among the influencing heavy metal adsorption parameters. Indeed, the adsorption of heavy metals in soil and water is ensured by clay minerals in minute proportions. Reference [27] shows that a clay dose of four to eight percent can achieve 70% removal of heavy metals. References [28, 29] show that the adsorption rate increases with increasing clay dose and [24] demonstrates that variation in clay mineral composition from region to region may likely affect remediation strength and required dosage. In the same perspective, previous research has shown that temperature is a key parameter that should not be overlooked during the heavy metal adsorption process. In fact, an optimum adsorption rate is obtained under ambient temperature conditions, although slightly lower or higher temperatures of 22–29°C may still be ideal [22, 25]. The works of [27, 30] show good results at relatively high temperatures 36°C, while some studies have observed an adsorption rate decrease as increasing temperature above 30°C [21, 31]. This probably indicates that very high temperatures promote desorption of heavy metals already adsorbed. Chemical adsorption reactions generally become faster as the temperature gradually increases and then decreases with a continuous increase in temperature [32, 33].

The montmorillonite layer structure is constituted by the stacking of two types of sheet [34–36]: an octahedral sheet O (MO_4 $(OH)_2$ with M as metal cation (Al, Mg)) sandwiched between two tetrahedral sheets T (SiO_4) often labelled T-O-T with an average layer thickness of around 10 Å. The layer charge is mainly related to existing isomorphic substitutions in the tetrahedral sheet (Al^{3+} and Si^{4+}) and/or octahedral ones (Mg^{2+}/Li^{+} and Al^{3+}/Mg^{2+}). To fill this charge deficit, compensator cations, coming mainly from the soil solution and inserted in the interlamellar space (IS), play the major role to achieve electrical neutrality of the sheet. Generally, exchangeable cations have a discrete hydrous sphere [37–39] which facilitates their insertion into IS and enables layer separation (exfoliation) and mineral dispersion (colloidal properties) in the soil solution and micro/macroscopic clay swelling properties. The insertion of the IS water molecule and exchangeable cations is accompanied by a progressive expansion of the basal spacing value $d(001)$ which is done by the discrete hydration state going from the dehydrated state $(0W, d(001) \approx 10\,\text{Å})$ to the strongly hydrated ones $(4W,\ d(001) \approx 21\,\text{Å})$ passing by the $1W(d(001) \approx 12.4\,\text{Å})$, $2W(d(001) \approx 15.4\,\text{Å})$, and $3W(d(001) \approx 18.2\,\text{Å})$ hydration states [37, 40]. On the other hand, the study of the clay structure finds its diversity in the multitude of possibilities of the adopted size scale, ranging from layer thickness (≈0.96 nm) along the $c*$ axis to an aggregate size around (≈1 μm) [41–43].

The application of clays in the context of deep geological waste confinement constitutes a well-developed research theme in this last decade given the multidisciplinary aspect of the identified problems [44–47]. The coating of these sites is ensured by a clay membrane, which, with its low permeability, is the main material used in the design and architecture of these landfills [48]. Clay membranes are now commonly used in the removal of toxic gases, coming from the landfill, and the trapping of trace metallic elements (TME), coming from a possible release. The use of compacted swelling clays as geological barriers is also considered under the multibarrier concept to ensure safe storage for several hundreds or thousands of years due to their high adsorption capacity for radionuclides, their low permeability resulting in very slow water molecule movement in the host rock, and a good capacity to conserve radionuclides by physicochemical adsorption [49]. One of the main components of engineered barriers is bentonite, which contains 70 to 95% of montmorillonite. The use of bentonite as a buffer in disposal galleries excavated between waste containers and tunnel walls achieves several strategic outcomes [49–54]. Several parameters overlap when designing underground facilities and disposal packages. As an example, we cite (i) the position of the repository in the middle of the geological formation, (ii) structures limiting environment mechanical disturbances, (iii) dimensioning limiting thermal disturbances, and (iv) durable disposal structures and packages. On the other hand, exploitation of clays in the context of the repository requires a deep understanding, based on the functionalities and the expected responses of these minerals, with respect to their natures, their abundance, their physicochemical properties, their location, their surrounding atmospheric conditions, their soil solution, the natural mechanical stress field, their soil hydrogeology/water chemistry, and the nature of the waste [55, 56]. Indeed, the main technical obstacles to radionuclide migration are mainly the disposal package and the surrounding bentonite. The bentonite (used as a buffer) interacts physically and chemically simultaneously with the soil and with the disposal package as a function of time, which induces the structure and intrinsic property changes, subsequently affecting the durability and safety of the material. According to the current concepts [50, 57], a bentonite barrier must retain its properties for several thousand years. Thus, when analyzing the prospects for the use of bentonite, it is necessary to consider not only their sorption properties in their natural state but also a possible loss of sorption capacity and other parameters necessary to preserve the stability of a barrier in "aggressive" environments. For that, we must study and predict the behavior of these minerals according to the constraints imposed by this "aggressive" environment. This response can vary from a significant transformation in structure and/or intrinsic properties towards performance affected by the nature of the stress [40, 58]. Despite the advances made and the results obtained in this context, several concepts related to permeability, the durability, the fatigue/stress of the geomembrane, the reversibility of the confinement process, and its relationship to the geomembrane performance and the material response under variable disturbance types remain unclear or even unanswered. Among the unresolved issues are the "obsolete" relationship between the crystallite size and the CEC, the link between

the nature and concentration of the radionuclide on the reversibility of the containment process, the mechanisms governing the physicochemical balance of clay and its environment, the relation between the crystallochemistry of the phyllosilicates and the geochemical constraints, etc.

This work focuses on the structural response, analyzed from the CEC, swelling properties, and porosity viewpoint when Na-montmorillonite was subjected to hydrogeological and/or geochemical constraints created at the laboratory scale. In this work, the constraint is the variation of the solid/liquid ratio between the soil solution (solvent) and the clay fraction (solute) and all resulting specific problems. Structural analysis is achieved through quantitative XRD analysis based on the modeling of the 001 reflections.

2. Materials and Methods

2.1. Baseline Material. Wyoming montmorillonite originates from Wyoming mineral deposit (USA), which belongs to the smectite family, with an octahedral CEC origin, and is used as a starting sample. The used reference montmorillonite sample (SWy-2) is a collected from the source clay repository of The Clay Minerals Society [59]. The half-cell montmorillonite structural formula is as follows [60]: $(Si^{4+}_{3.96}, Al^{3+}_{0.04})(Al^{3+}_{1.53}, Fe^{3+}_{0.18}, Mg^{2+}_{0.26}, Ti^{4+}_{0.01})O_{10}(OH)_2(Ca^{2+}_{0.07}, K^{+}_{0.01}, Na^{+}_{0.2})$.

2.2. Pretreatment. A pretreatment of the starting material to prepare a Na-rich montmorillonite suspension, labelled Swy-Na, is prepared according to a classical protocol detailed by [61]. This process is assured by dispersing ~10 g of solid in ~100 mL of 1 M NaCl solution. Indeed, SWy-2 suspensions in this saline solution were shaken mechanically for 24 h before separation of the solid fraction by centrifugation and addition of fresh saline solution. These steps were repeated five times to ensure a complete cation exchange. Excess salt was washed out by four 24 h cycles that included sedimentation, removal of the supernatant, and immersion in deionized water. The recovered clay suspension is first dried in an oven for 24 h at 60°C, then grinded, and weighted.

2.3. Exchangeable Cations. Two heavy metal cations (Ba^{2+} and Ni^{2+}) were the subject of the cation exchange process. The cation preference is explained by the wonderful abundance of the latter in industrial and radioactive waste and the specific characteristics of each one [46, 58].

2.4. Variable Solid/Liquid Ratio. The solid/liquid ratio (R_{M-i}) fluctuation is assured by varying the volume of the (0.5 M) $BaCl_2$ and (0.5 M) $NiCl_2$ solutions associated with a constant mass (0.1 g) of the starting dried SWy-Na powder. The R_{M-i} values for both exchangeable cations (Ba^{2+} and Ni^{2+}) are reported in Table 1. This ratio is determined after a simple homogenization of the relation mass (solid fraction) on volume (liquid fraction) which takes the dimensions of a concentration ($g{\cdot}L^{-1}$) in the logic.

Table 1: R_{M-i} solid/liquid ratio. M: Ba^{2+} or Ni^{2+}; R_{M-i} (i = 1, 2, 3, 4, 5, and 6).

i	1	2	3	4	5	6
R_{Ba-i}	9.16	7.49	6.20	5.50	4.25	3.12
R_{Ni-i}	7.54	5.21	4.08	3.10	2.29	1.74

In addition, it is necessary to take into account the porous texture of clay and its very large internal specific surface area which gives it a considerable internal volume.

To obtain dimensionless ratio values, a simple calculation was carried out on the volume of each solution ($BaCl_2$ and $NiCl_2$) to transform it into mass.

The main objective is to obtain an oriented R_{M-i} ratio series which allows us to investigate the effect of the series fluctuation on the structural response for each cation individually. After that, a comparison between the effects of the exchangeable cation nature can be discussed.

2.5. Cation Exchange Process. After purification and impurity removal from the baseline materials (SWy-Na), the cation exchange process for Ba^{2+} and Ni^{2+} cations is started with a variable solid/liquid ratio (R_{M-i}) as shown in Figure 1. The same experimental protocol is approved for each series of R_{M-i} values. Each sample is subjected to 48-hour mechanical shaking to ensure the exchange process, followed by centrifugation at 6000 rpm. After recuperation of the solid fraction, the salt excess (chloride ions) is removed by washing with distilled water accompanied by an $AgNO_3$ test. The cation exchange is controlled by XRD analysis. Therefore, the obtained samples are referred to as R_{Ba-i} and R_{Ni-i} (i = 1, 2, 3, 4, 5, and 6).

The cation exchange process suggests a succession of mechanical shaking, centrifugation, and washing cycles with well-defined durations to ensure achievement of the process and to reach equilibrium [46]. This approach is not really respected in this work considering that the centrifugation and washing cycles will affect the main parameter to be investigated which is the solid/liquid ratio, and subsequently, they will really distort the possible reached equilibrium. To overcome experimentally this ambiguity and so as not to disturb the reached equilibrium imposed by the R_{M-i} solid/liquid ratio, several approximations have been considered. Indeed, there is an increase over time in the single mechanical stirring sequence (48 h) with a relatively high concentration of the metallic solution (0.5 M) and a single extended washing cycle (24 h) after possible cation exchange process.

Oriented slides were prepared for all complexes, by depositing the sample suspension on a glass slide and then drying it at room temperature for a few hours to obtain an air-dried preparation. The results obtained by [40, 46, 58, 62–65] are adopted for a possible comparison in the case of reference montmorillonite exchanged Ba^{2+} and Ni^{2+}. It remains to be noted that the developed experimental approach was respected for the two exchangeable cations and the quantitative characterization of the ion exchange process is ensured by the XRD analysis.

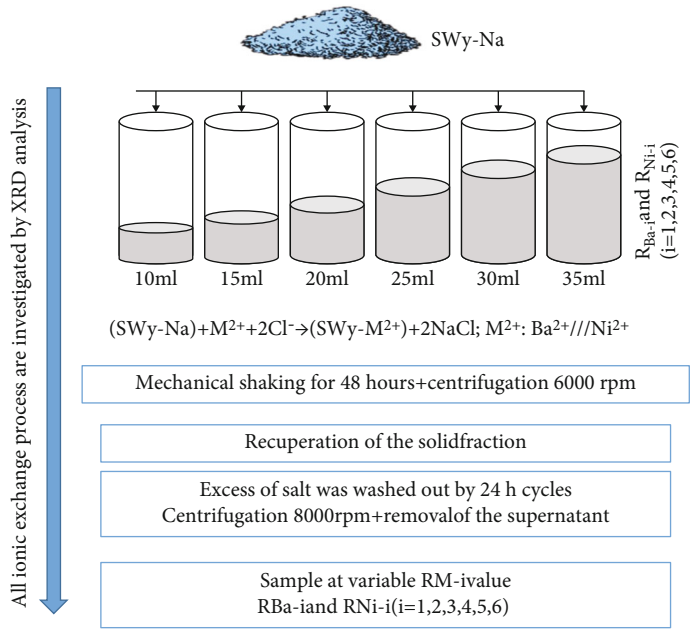

Figure 1: Experimental protocol for the exchange process with the variable solid/liquid ratio. M: Ba^{2+} or Ni^{2+}.

2.6. X-Ray Diffraction (XRD). XRD is the basic analysis method for the structural characterization of clay minerals. A Bruker D8 ADVANCE X-ray diffractometer (Bruker AXS GmbH, Karlsruhe, Germany) with a monochromatic CuKα radiation ($\lambda = 0.15406$ nm) was used to investigate the crystalline structures at 40 kV and 20 mA.

The usual scanning parameters were 0.01 $2\theta^\circ$ as the step size and 6 s as the counting time per step over the explored angular range. Indeed, the XRD profiles were recorded in the $2\theta^\circ$ range from 3 to 35 for all specimens. The Scherrer equation was used to determine the average crystallite size. All records are made at room temperature under atmospheric pressure. XRD investigations were directed by the correlation between qualitative and quantitative analyses.

2.6.1. Semiquantitative XRD Analysis. The identification and characterization of all studied samples are carried out by XRD analysis, which is a basic technique for the structural change investigation [66–68]. In practice, XRD analysis is carried out in two complementary steps. The first step consists of a semiquantitative way focusing on the qualitative identification of the mineral type based on some parameters such as the basal spacing $d(001)$ from the first-order (001) Bragg reflections, the FWHM (full width at half maximum) of the 001 reflection, and the deviation rationality parameter (ξ) of the 001 reflection position [49].

Indeed, this parameter is calculated as the standard deviation of the $l \times d(001)$ values calculated for the X_i measurable reflections over the explored $2\theta^\circ$ CuKα angular range [69]. The second step consists of the use of a specific quantitative XRD analysis to access a realistic description of the structure. Indeed, this goal was achieved using an indirect method based on the comparison of experimental XRD patterns to calculated ones from theoretical ones.

The semiquantitative parameter indication, combined with the profile geometry (i.e., symmetric or asymmetric X-ray peaks) description, provided preliminary information about the hydration evolution and IS content of the studied complex all over the explored R_{M-i} value.

The qualitative analysis remains insufficient for a deep investigation targeting nanometric structural information at the basic layer scale (i.e., position and arrangement of exchangeable cations M^{2+} with H_2O molecules in the IS along the $c*$ axis, crystallite heterogeneities, crystallite defaults, and layer interstratification); for these reasons, a quantitative XRD analysis was performed.

2.6.2. XRD Profile Modelling: Theoretical Diffracted Intensity and Modelling Strategy. The XRD modeling method is used to quantify the mixed layer structure, the layer hydration state, CEC fluctuations, optimum IS configuration, crystallite size, average layer number per crystallite, and structural heterogeneities. The modelling approach is based on a matrix formalism initially developed by [70] and whose expression of the diffracted intensity along the (001) rod belonging to the reciprocal space is given by [70]:

$$I_{001}(2\theta) = L_p \mathrm{Spur}(\mathrm{Re}\,[\varnothing][W]\left\{[I] + 2\sum_{n}^{M-1}\left[\frac{(M-n)}{n}\right][Q]^n\right\}, \quad (1)$$

where Re means the real part of the final matrix, Spur is the sum of the diagonal terms of the real matrix, Lp is the Lorentz-polarization factor, M is the number of layers per stack, $n = 1, \cdots, 1 - M - 1$, $[\Phi]$ is the structure factor matrix, $[I]$ is the unit matrix, $[W]$ is the diagonal matrix of the proportions of the different kinds

Table 2: The z atomic coordinates within the 2 : 1 layer framework along the $c*$ axis [70].

Atom type	O_1	O_2	O_3	O_4	O_5	O_6	OH_1	OH_2	Si	Si	Al
Number	2	1	2	2	1	2	1	1	2	2	2
Zn (Å)	0	0.20	2.25	4.31	6.26	6.59	1.98	4.28	0.59	6.04	3.43

of layers, and $[Q]$ is the matrix representing the interference phenomena between adjacent layers.

The modelling approach allowed us to determine the abundance of the different layer types (W_i), the stacking mode of the different kinds of layers, and the mean number of layers per coherent scattering domain (CSD) [40]. Within a CSD, the stacking of layers is described by a set of junction probabilities (P_{ij}). Briefly, the relationship between probabilities and the W_i abundance of two different types of layers (i and j) can be summarized as follows: (i) the segregation tendency is given by $W_i < P_{ii}$ and $W_j < P_{jj}$, (ii) the total demixion is obtained for $P_{ii} = P_{jj} = 1$, (iii) the regular tendency is obtained if $W_i < P_{ji} < 1$ and $W_j < P_{ij} < 1$, and (iv) finally, the limit between the last distribution labelled chaotic/or random distribution is obtained when $W_i = P_{ji} = P_{ii}$ and $W_j = P_{ij} = P_{jj}$ with $\sum W_i = 1$ and $\sum P_{ij} = 1$ [70, 71].

The fitting strategy consists of reproducing the experimental XRD pattern using a main homogeneous structure. If necessary, additional contributions to the diffracted intensity are introduced to account for improve agreement between calculated and experimental patterns (i.e., if we have more one main structure, a mixed layer structure can be introduced).

The presence of two mixed layer structures (MLSs) does not imply that two populations of particles are physically present in the sample [46, 72, 73]. Therefore, layers with the same hydration state present in the different MLSs contributing to the diffracted intensity are assumed to have identical properties (chemical composition, layer thickness, and z coordinates of atoms). The details of the XRD modelling approach are sufficiently and widely explained in previous works by [32, 33, 40, 46, 72, 73].

The z atomic coordinates within the 2 : 1 layer framework (tetrahedral and octahedral sheet) in the case of this study are reported in Table 2.

The z coordinates of the IS content (exchangeable cation, molecules, etc.) are optimized, during the modeling process, to improve the agreement quality. This later is controlled using the unweighted Rp parameter [52]:

$$\mathrm{Rp} = \sqrt{\frac{\sum [I(2\theta_i)\mathrm{obs} - I(2\theta_i)\mathrm{calc}]^2}{\sum [I(2\theta_i)\mathrm{obs}]^2}}. \quad (2)$$

The optimum quantitative structural characterization of a given sample necessarily involves the search for an agreement between the calculated profiles and experimental ones. Regardless of the hydration state type, the metallic exchangeable cations (per half-unit cell) are positioned at the center of the IS along the $c*$ axis. This configuration respects the provided literature data [38, 39, 73].

2.7. BET and BJH Pore Size Distribution Analyses. The nitrogen adsorption–desorption measurements (BET method) onto the clean surface of dry solid powders are used to determine the surface area (SA) (using the BET equation) and the pore size distribution (PSD) of porous materials such as montmorillonite.

In this case, powders are obtained after drying each sample. Physical gas adsorption is often the technique of choice for examining the pore characteristics of materials [74]. The technique determines the amount of gas adsorbed; this is a direct indication of the porous properties and, therefore, the overall structure of the material [75, 76]. Adsorption isotherms were performed at 77 K and at the relative pressure up to $P/P0 \sim 0.95$. Adsorbed nitrogen and oxygen were removed under reduced (vacuum) pressure at 100°C for 8 h before measuring SA and PSD.

A BET-specific surface area and PSD of the studied sample, under each R_{M-i} value, were determined using a Quantachrome NOVA 2000e series volumetric gas adsorption instrument, which is a USA-automated gas adsorption system using nitrogen as the adsorptive. The analysis procedure is automated. The PSD was determined by the BJH method [76–78] to the desorption section of the isotherms of nitrogen at 77 K, assuming the pores to be cylindrical in shape [79].

3. Results and Discussion

3.1. Qualitative and Quantitative Description of Experimental XRD Patterns of the Baseline Sample: Swy-Na. The XRD experimental profile of the starting SWy-Na complex (Figure 2) shows three characteristic reflections ($n = 1$, 2, and 4). The 001 reflection is located at $2\theta = 7.04°$ ($d(001) = 12.54$ Å) indicating probably a $1W$ hydration state (Table 3). The investigation of the calculated FWHM and the ξ parameter value confirms the homogeneous character which is consistent with the results obtained by [73] on the same sample. Indeed, the Na exchangeable montmorillonite (SWy-2-Na) sample is well studied earlier since it is a reference sample [33, 37–40, 45, 61, 73]. Our objective in this stage of the study was to refine the obtained results related to the SWy-Na sample with those founded in the literature.

The mixed layer structure (MLS) used to obtain the best agreement, between experimental and theoretical XRD patterns, shows a heterogeneous hydration character which is displayed by the coexistence of three hydrous layer types (Table 4). Indeed, an unfair contribution of different layer types, in favor of the $1W$ layer state, is used. The IS water molecule distribution respected previous works [32, 37–39, 72] with one water sheet located in the middle of the IS for the $1W$ phase and two water sheets on either side of the middle of IS for the $2W$ hydration state. Regardless of the

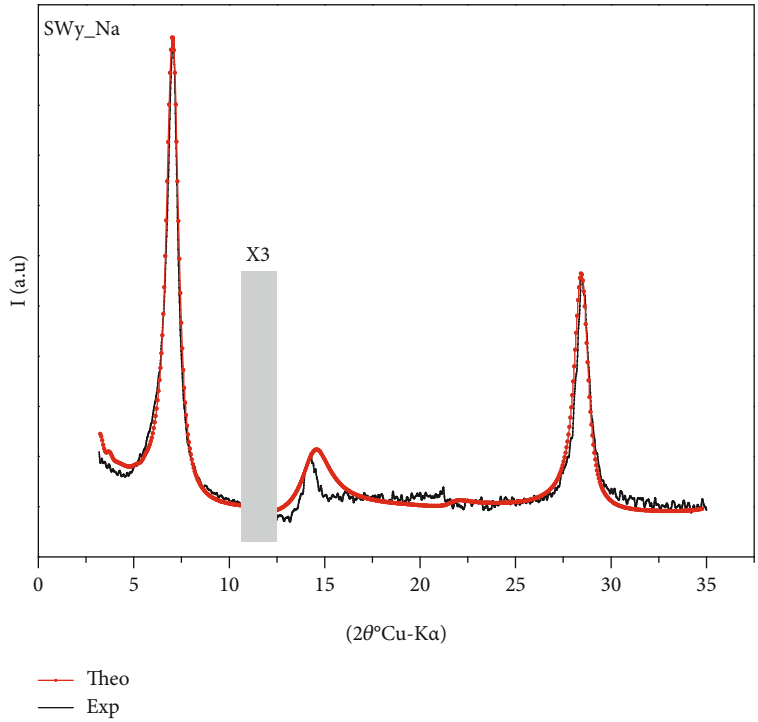

Figure 2: Best agreement obtained between theoretical and experimental profiles in the case of the SWy-Na complex.

Table 3: Qualitative XRD investigation in the case of the SWy-Na sample.

Sample	$2\theta^{\circ}$	$d(001)$ (Å)	FWHM ($2\theta^{\circ}$)	Aver. cryst. size D (Å)	ξ (Å)	Hydration characters
SWy-Na	7.04	12.54	0.69	20.13	0.086	Homogenous

hydration state type, the Na exchangeable cations (per half-unit cell) are positioned at the center of the IS along the $c*$ axis. This configuration respects the provided literature data [37–39]. The average layer number per crystallite is 15.

Structural parameters summarized in Table 4 show a discretization of the hydration heterogeneity indicating the interstratification of the different hydration state types ($0W$, $1W$, and $2W$) within the same layer. Physically, this can be translated into fluctuations in the layer thickness as a function of the extended lateral specific surface area, which affects the average of the crystallite size, the clay particle size, and the porosity value.

3.2. Qualitative Description of Experimental XRD Patterns of the SWy-Ba Sample. Experimental XRD patterns, in the case of SWy-Ba, obtained by varying the constraint strength $R_{\mathrm{Ba}-i}$ ($i = 1, 2, 3, 4, 5$, and 6) are summarized in Figure 3. For $R_{\mathrm{Ba}-i}$ values ranging from 1 to 4, the experimental XRD patterns are characterized by a main 001 reflection ($d(001) = 12.62$ Å) probably attributed to high Na^{+} cation residue from the starting sample. This deduction is essentially based on the works of [39, 58] which show that a complete cationic exchange in the case of barium is accompanied by the insertion of two water layers in IS and thereafter a minimum basal distance of 15 Å.

The 001 reflection is accompanied by a shoulder towards small angles around $d(001) = 15.23$ Å and probably attributed to the $2W$ hydration state synonym of the presence of a minor Ba^{2+} cation fraction in IS. Generally, the observed asymmetric 001 reflection reflects the coexistence of several hydration states within the stack and/or an incomplete (partial) cation exchange. The exploitation of the FWHM and ξ parameter values confirms this supposition (Table 5).

For $R_{\mathrm{Ba}-5}$ and $R_{\mathrm{Ba}-6}$, the 001 reflections are more symmetric with a remarkable shoulder (around 15.23 Å) intensity decrease explained, at this stage, by the dominance of the 1 W hydrated fraction attributed to the starting sodium. The sodium cation presence in the IS in this situation is explained by the exchange process failure, which is attributed to the always existing possibility of the natural cationic exchange and which results in a minor fraction of Ba^{2+} and the experimentally induced cation exchange by the intensity and the mechanical stirring time. This homogeneity trend results in low FWHM and ξ parameter values [72, 73]. This result is not consistent with previous works focusing the same exchanged Ba^{2+} sample. Indeed, the works of [38, 39, 58] show that the associated XRD patterns are generally characterized by homogeneous $2W$ phases with $d(001) \approx 15.2$ Å. The objective of this anterior work was to obtain and characterize reference specimen exchanged

Table 4: Optimal structural parameters obtained from quantitative XRD analysis in the case of the SWy-Na sample.

Layer types	%	L.Th $d(001)$	n_{H2O}	z_{H2O}	$n_{exch.cat\_Na+}$	$z_{exch.cat\_Na+}$	W_A	P_{AA}	M	Rp
$0W$	15	10.50	0	0	0.0495	8.5				
$1W$	70	12.40	2	9.8	0.2310	9.8	1	1	15	4.31%
$2W$	15	15.40	1	11.3	0.0495	12.6				
			1	13.9						

L.Th: layer thickness (Å); $d(001)$: basal spacing value (Å); n_{H2O}: number of water molecules; z_{H2O}: position of water molecules along IS thickness; $n_{exch.cat}$: number of compensating cations; $z_{exch.cat}$: position of compensating cations along IS thickness; W_A: relative abundance of the A-type layer; P_{AA}: probabilities of the successive A-type layer; M: average layer number per stack.

Ba^{2+}. This study seeks, rather, to characterize a limit of the cationic exchange, under variation of the solid/liquid ratio, which, of course, makes the difference and the novelty of the work.

3.3. Qualitative Description of Experimental XRD Patterns of the SWy-Ni Sample. Regardless of the R_{Ni-i} value, the experimental XRD patterns (Figure 3) in the case of SWy-Ni complexes show a main 001 reflection characterizing an intermediate $1W/2W$ hydration state with $2W$ hydration state trend $d(001) = 14.43$ Å. Bibliographic data [22, 46] demonstrate that, under room atmospheric conditions and in the case of Ni^{2+} exchangeable cations, a homogeneous 2 W hydration state is developed when SWy-Na is used as starting material. This result is not really respected in our case even for an initial R_{Ni-1} value (i.e., in the absence of any constraint). Indeed, a right-handed profile asymmetry towards the large angles ($2\theta = 7.1°$; $d(001) = 12.62$ Å), which is ascribed to the minor 1 W hydration state phase, was observed independently of the applied constraint strength. The appearance of this profile asymmetry seems to be unaffected by the variation in the solid/liquid ratio. These observed heterogeneities are confirmed by fairly close and high values of the FWHM and ξ parameters (Table 5). This interpretation remains qualitative since the coexistence of two or more phases cannot be demonstrated by simple semi-quantitative calculation.

Several characteristics, at this stage, remain undefined, at least by way of example but not limited: (i) the$d(001) = 14.43$ Åis explained by an incomplete exchangeable site saturation or a maximum hydration process due to the layer exfoliation process, (ii) the existence of the minor layer population at 12.62 Å is it attributed to an unfinished exchange process, and in this case, why or to a partial exchange and with stirring time, it will evolve towards the$2W$state properly, and (iii) what is the relation between the coexistence of two layer types and the effect of the layer stacking on the experimental diffractogram. Quantitative XRD analysis must give accurate and precise answers.

3.4. Modeling of X-Ray Diffraction Profiles

3.4.1. Case of the SWy-Ba Sample. The qualitative XRD analysis suggested, whatever the R_{Ba-i} strength, a heterogeneous hydration behavior. This interstratification was approved by the 001 reflection modelling approach which supposes the coexistence of three different hydration states (e.g., $0W$, 1 W, and $2W$). To improve the agreement between the calculated and experimental patterns (Figure 3) and for each R_{Ba-i} ($i = 1, \cdots, 6$) value, the proposed mixed layer structure is theoretically decomposed into different layer populations (i.e., $0W$_L.Th ≈ 10.00 Å), $1W$_L.Th ≈ 12.20 Å, and $2W$_L.Th ≈ 15.20 Å) stacked according to specific succession probability laws. The structural parameters associated with this modelling approach is summarized in Table 6. The proposed MLS are obtained by the weighted layer type populations which are supposed to have identical chemical composition, identical layer thickness, and identical z coordinates of the atoms [80].

The CEC of the starting materials is partially saturated by Na^+ and Ba^{2+} cations seen that, under room conditions, sodium always presents a $1W$ hydration state [73]; on the other hand, the barium presents $2W$ hydration ones [58].

The fitting quality is controlled by the Rp parameter. The phase ponderation is in favor of the 1 W hydration state attributed to the Na^+ cation whatever the R_{Ba-i} ($i = 1, \cdots, 6$) value is. The $2W$ phase minor contribution, in the used MLS, describes clearly the observed 001 reflection asymmetry and confirms the partial barium cation exchange process.

3.4.2. Case of the SWy-Ni Sample. The best fit of all experimental XRD patterns (Figure 3) obtained along the R_{Ni-i} range is obtained through theoretical models with a main interstratified structure using three MLSs including various relative proportions of the layer with different hydration states (Table 6). This variability confirms the heterogeneous hydration character and the intermediate $1W/2W$ observed hydration phase regardless of the R_{Ni-i} value.

In detail, a minor contribution of the $0W$ phase, not exceeding 3% but omnipresent, is observed regardless of the solid/liquid ratio. On the other hand, the dominance of the $2W$ hydration phase with weighting fluctuations is the proof of a cation exchange process. Indeed, the $2W$ hydration phase implemented in the theoretical model was mandatorily assigned to the fraction whose CEC is saturated Ni^{2+} [46]. The presence of the $1W$ layer hydration state population (where the CEC is saturated by the starting Na^+) is interpreted by the existence of a (fairly large) fraction "unconcerned" to the applied constraint (Figure 4).

The obtained agreements between theoretical and experimental profiles (Rp ≈ 5 to 7%) are generally acceptable, despite the misfit observed after widening (zoom 10x) of the peaks around 30° (2θ). In fact, this disagreement can

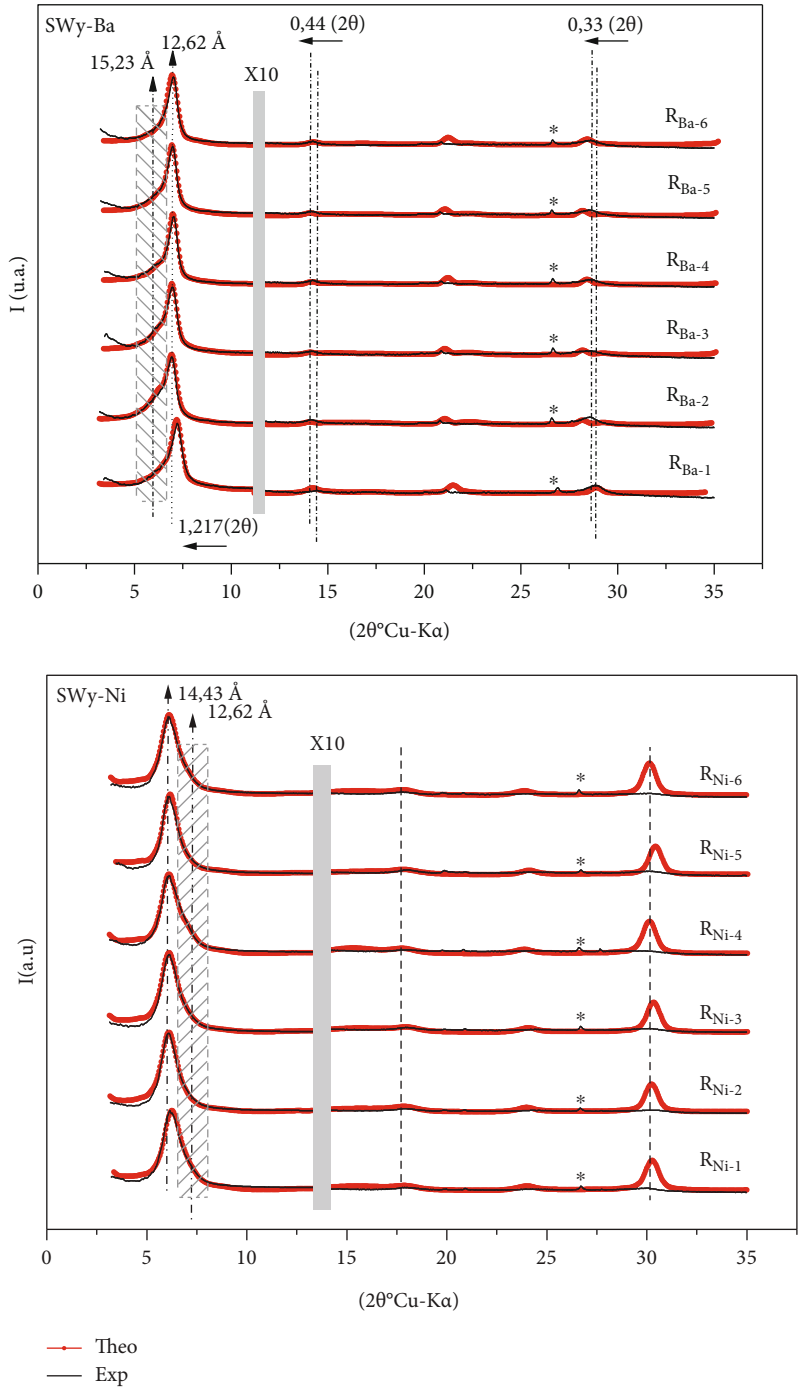

Figure 3: Best agreement between theoretical and experimental XRD profiles obtained in the case of the SWy-Ba and SWy-Ni samples. * Halite (NaCl).

be broken down into a positional agreement and a diffracted intensity disagreement probably linked to the distribution and the number of water molecules in the SI. This disagreement led us to explore the areas of large angles, later to find an eventual link between CEC saturation, IS filling, and hydration heterogeneities degree.

The logical increase of the Rp factor in the case of the Ba exchanged sample finds its explanation in the 001 reflection asymmetry (which contains all structural defaults), the elevated FWHM value, and the ξ rationality parameter. Theoretically, this result is linked to the variability of possible MLS configurations allowing a good fit of the 001 reflection.

The exploitation of the W_A, P_{AA}, M, and Rp factor values allowed us to characterize a specific distribution of the normalized n layers within the crystallites according to the generated stacking modes and the contribution of each

Table 5: Qualitative XRD investigation in the case of the SWy-Ba and SWy-Ni samples.

Samples	R_{M-i}	$2\theta^{\circ}$	$d(001)$ (Å)	FWHM ($2\theta^{\circ}$)	D (Å)	ξ (Å)	Characters
SWy-Ba	R_{Ba-1}	7.21	12.24	1.08	12.86	0.151	Interstratified
	R_{Ba-2}	6.94	12.73	1.19	11.67	0.281	
	R_{Ba-3}	6.96	12.68	1.08	12.86	0.192	
	R_{Ba-4}	7.03	12.57	0.97	14.34	0.114	
	R_{Ba-5}	6.98	12.66	0.80	16.15	0.097	
	R_{Ba-6}	7.02	12.59	0.78	17.81	0.094	
SWy-Ni	R_{Ni-1}	6.15	14.36	1.10	12.62	0.444	Interstratified
	R_{Ni-2}	6.12	14.43	0.97	14.31	0.426	
	R_{Ni-3}	6.13	14.40	1.02	13.61	0.449	
	R_{Ni-4}	6.12	14.43	1.17	11.87	0.406	
	R_{Ni-5}	6.11	14.45	0.94	14.77	0.456	
	R_{Ni-6}	6.10	14.48	1.10	12.62	0.546	

R_{M-i} ($i = 1, \cdots, 6$) solid/liquid ratio (M; Ba or Ni cations); D: aver. cryst. size.

phase. This layer statistical representation can help in understanding the low or the high CEC sensitivity (of the starting sample) towards the soil solution concentration regardless of the R_{M-i} strength.

3.5. Evolution of the n_{H2O}, 0W, 1W, and 2W Amounts versus Constraint Strength

3.5.1. Case of the SWy-Ba Sample. For a given R_{M-i} value, the sample hydration state is governed by the cation nature, the layer charge value, and the layer charge location [37–39, 41, 81–84]. All studied samples belong to the Wyoming montmorillonite specimen characterized by the same layer charge and the charge location value. The exchangeable cation nature and abundance (variable solid/liquid ratio) are at the origin of this specific hydration behaviors. The water affinity of the exchangeable cation is related to the ionic potential defined by the ratio of the valence of the cation to its ionic radius [85]. This potential increases as the affinity of the cation for water rises. Thus, a cation like barium having a high water affinity will generate a $2W$ hydration state ($d(001) \approx 15.2$ Å) [38, 39]. On the contrary, cations like sodium or potassium having a lower affinity for water will exhibit generally monohydrate states $1W$ ($d(001) \approx 12.2$ Å). With quantitative XRD analysis, a discretization of the IS content is achieved. Indeed, the evolution of the H_2O molecules, fraction per half-unit cell, versus constraint strength is determined (Figure 5(a)). For the SWy-Ba sample, an overall linear decrease in the number of water molecules as a function of the increase in the solid/liquid ratio is observed. Using a linear regression approach, a further equation related to the decrease in the amount of H_2O molecules per half-unit cell (n_{H2O}) versus the R_{Ba-i} value can be developed. The behavior and evolution of the n_{H2O} amounts versus constraint strength are perfectly described by these regressions. Indeed, from the observed dependence of the latter parameter on the R_{Ba-i} value, the equations were derived which allow the quantification of the hydration behavior when increasing the solid/liquid ratio. In the case of Ba^{2+} cation,

$$n_{H2O} = 2.657 - 0.285 * R_{Ba-i}, \quad \text{with } i = 1, 2, 3, 4, 5, \text{and } 6. \tag{3}$$

The n_{H2O} fluctuation (Δn_{H2O}) range varies from 2.3 to 0.8, with a negative slope of −0.285 (zones I and II).

For the first three values of R_{Ba-i} ($i = 1, 2, 3$) (zone I), a slow decrease of n_{H2O} fluctuation is observed ($\Delta n_{H2O} = 0.45$). This fluctuation accelerates for $i$values > 3 (zone II) to reach $\Delta n_{H2O} = 0.98$.

Physically, this is in accordance with the experimentally observed variations on the intensity and the shape of the 001 reflection.

In fact, up to R_{Ba-3} (zone I), the appearing shoulder towards the low 2θ values is attributed to a partial CEC saturation with Ba^{2+} cation; a fairly large crystallite fraction presents a $2W$ hydration state indicating the interlayer Ba presence. Also, the global description of the crystallite's nature shows a coexistence of two-layer type populations with a different IS filling characterized by a dominance of sodium-saturated clay particles. Thus, it is like a barium cation exchange beginning, which did not persist for high values of R_{Ba-i}. For $i$values > 3 (zone II), the n_{H2O} trends towards weakly hydrated states ($1W$) are noted. This results in the conservation of the starting hydration state and the practical absence of cationic exchange.

3.5.2. Case of the SWy-Ni Sample. The same study was carried out for nickel cations. The obtained results show a completely different behavior from that of the barium case, which was expected, but a considerable difference was noted. Indeed, the amount of H_2O molecules per half-unit cell (n_{H2O}) always respects a linear variation according to the intensity of the applied constraint (Figure 5(b)). A similar

Table 6: Structural parameters of SWy-Ba and SWy-Ni complexes.

R_{M-i}	%MLS	xW_excha.cat	L.Th (Å)	n_{H2O}	W_A	P_{AA}	M	M_{tot}	%Rp
R_{Ba-1}	54.3	1W_Na	12.2	0.5	1	1	12	9	8.49
	39.1	1W_Ba	12.2	1	1	1	5		
	3.25	1W_Ba	12.2	0.1	0.4	0.5	5		
		2W_Ba	15.2	0.3	0.6				
				0.3					
	3.35	0W_Na	10	0	1	1	4		
R_{Ba-2}	52.36	1W_Na	12.2	0.8	1	1	12	9	7.12
	33.84	1W_Ba	12.2	0.1	0.7	0.59	5		
		2W_Ba	15.2	0.1	0.3				
				0.1					
	12.30	1W_Ba	12.2	0.4	0.5	0.5	5		
		2W_Ba	15.2	0.3	0.5				
				0.3					
	1.5	0W_Na	10	0	1	1	4		
R_{Ba-3}	59.44	1W_Na	12.65	0.5	1	1	12	9	7.43
	39.52	1W_Ba	12.2	0.15	0.7	0.71	5		
		2W_Ba	15.2	0.1	0.3				
				0.1					
	1.04	0W_Na	10	0	1	1	4		
R_{Ba-4}	68.61	1W_Na	12.55	0.4	1	1	12	10	8.33
	30	1W_Ba	12.2	0.1	0.7	0.72	5		
		2W_Ba	15.2	0.1	0.3				
				0.1					
	1.39	0W_Na	10	0	1	1	4		
R_{Ba-5}	65.21	1W_Na	12.65	0.7	1	1	12	10	6.84
	33.52	1W_Ba	12.2	0.1	0.7	0.6	5		
		2W_Ba	15.2	0.1	0.3				
				0.1					
	1.27	0W_Na	10	0	1	1	4		
R_{Ba-6}	72.22	1W_Na	12.6	0.5	1	1	12	10	8.66
	25.48	1W_Ba	12.2	0.1	0.7	0.7	5		
		2W_Ba	15.2	0.1	0.3				
				0.1					
	2.30	0W_Na	10	0	1	1	4		
R_{Ni-1}	70.47	1W_Ni	12	0.1	0.3	0.3	8	7	4.37
		2W_Ni	15	0.1	0.7				
				0.1					
	27.57	1W_Ni	12.5	0.5	0.7	0.7	5		
		2W_Ni	15.5	0.8	0.3				
				0.8					
	1.96	0W_Na	10	0	1	1	5		

Table 6: Continued.

R_{M-i}	%MLS	xW_excha.cat	L.Th (Å)	n_{H2O}	W_A	P_{AA}	M	M_{tot}	%Rp
		1W_Ni	12.5	0.1	0.3				
	77.91	2W_Ni	15.5	0.1	0.7	0.3	8		
				0.1					
R_{Ni-2}		1W_Ni	12.5	0.6	0.6			7	5.74
	20.38	2W_Ni	15.5	0.85	0.4	0.65	5		
				0.85					
	1.71	0W_Na	10	0	1	1	5		
		1W_Ni	12.5	0.1	0.3				
	76.45	2W_Ni	15.5	0.1	0.7	0.3	8		
				0.1					
R_{Ni-3}		1W_Na	12.5	0.7	0.7			7	3.39
	22.01	2W_Na	15.5	0.9	0.3	0.7	5		
				0.9					
	1.54	0W_Na	10	0	1	1	5		
		1W_Ni	12.5	0.1	0.3				
	73.33	2W_Ni	15.5	0.1	0.7	0.3	8		
				0.1					
R_{Ni-4}		1W_Na	12.5	0.68	0.82			7	4.86
	24.59	2W_Na	15.5	1	0.18	0.8	5		
				1					
	2.08	0W_Na	10	0	1	1	5		
		1W_Ni	12.5	0.1	0.3				
	82.77	2W_Ni	15.5	0.1	0.7	0.2	8		
				0.1					
R_{Ni-5}		1W_Na	12.5	0.8	0.75			7	6.09
	15.01	2W_Na	15.5	1.1	0.25	0.7	5		
				1.1					
	2.22	0W_Na	10	0	1	1	5		
		1W_Ni	12.5	0.1	0.3				
	78.67	2W_Ni	15.5	0.1	0.7	0.35	8		
				0.1					
R_{Ni-6}		1W_Na	12.5	1	0.8			7	4.19
	19.20	2W_Na	15.5	1.1	0.2	0.75	5		
				1.1					
	2.13	0W_Na	10	0	1	1	5		

xW_excha.cat: layer type and the associated exchangeable cation; L.Th: layer thickness in Å. 2W, 1W, and 0W are attributed to the layer hydration state. n_{H2O}: the number of H_2O molecules per half-unit cell; z_{H2O}: the position along the $c*$ axis of the H_2O molecule is fixed to 9.5 Å and 11.3 Å - 13.9 Å for the 1W and 2W hydration states, respectively. The position of exchangeable cations per half-unit cell calculated along the $c*$ axis is fixed to 8.30 Å, 9.50 Å, and 12.25 Å for the 0W, 1W, and 2W hydration states, respectively [80]. $n_{excha.cat}$: the number of exchangeable cation per half-unit cell is fixed to 0.33 (for Na^+ cation) and 0.165 (for Ba^{2+} and Ni^{2+} cation), indicating full saturation of the cation exchange capacity (CEC).

equation to that found in the case of barium has been developed according to a linear regression approach:

$$n_{H2O} = 2.152 + 0.219 * R_{Ni-i}, \quad \text{with } i = 1, 2, 3, 4, 5, \text{and } 6, \tag{4}$$

which shows a high sensitivity of water response to the presence of the Ni^{2+} cation in the solution. Moreover, this result confirms the XRD analysis, which shows a quasiachievement of the cation exchange process whatever the value of R_{Ni-i} is.

3.6. Evolution of the Layer Type Abundance versus Constraint Strength. An "ephemeral" cation exchange

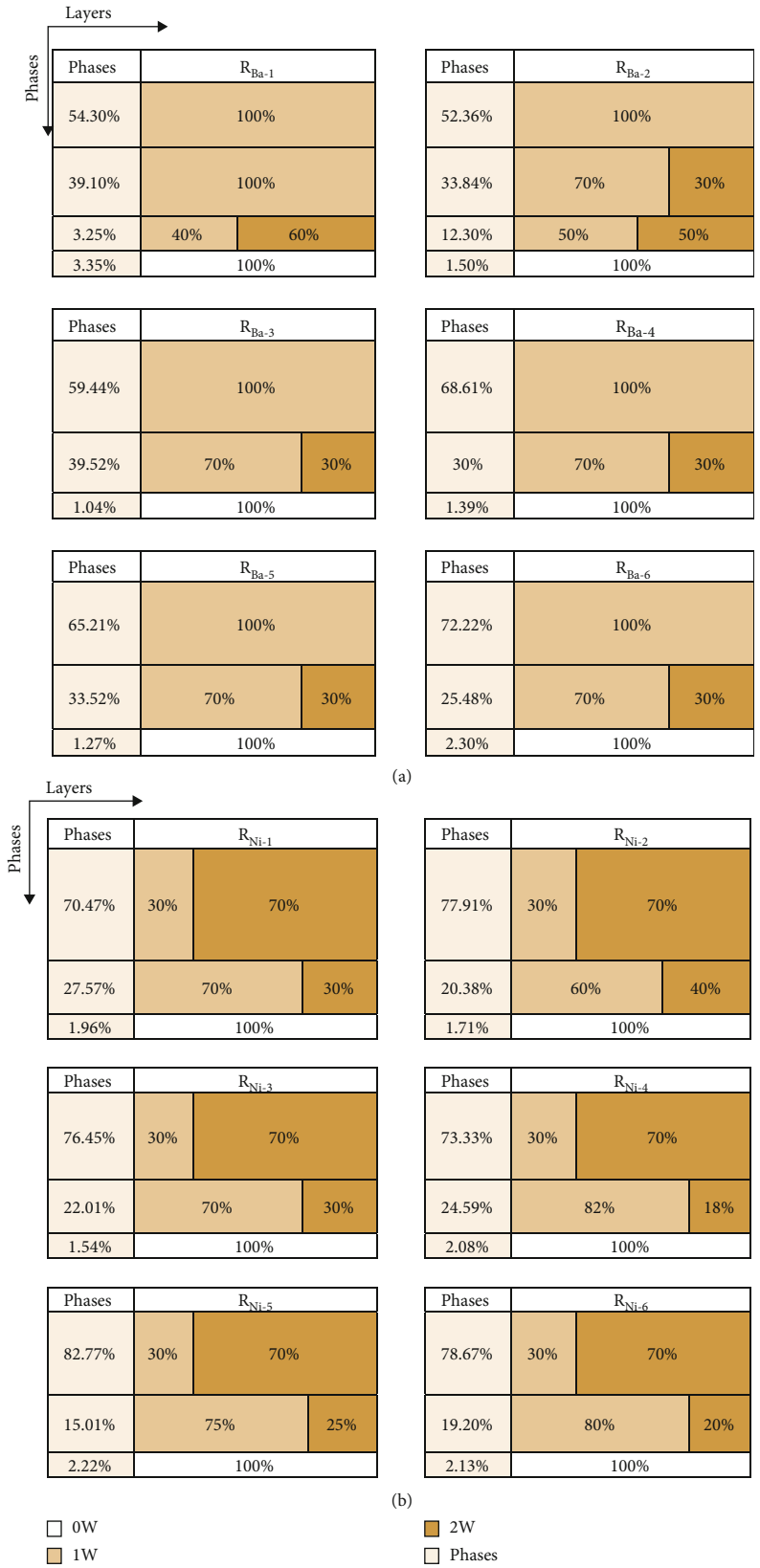

Figure 4: Graphic Representation of the hydration state in the case of SWy-Ba (a) and SWy-Ni (b) samples via modelling of X-ray diffraction. Colors white, light-brown, and dark-brown represent the type $0W$, $1W$, and $2W$ layer hydration states, respectively. Each line thus represents a layer with his own hydration state. The configuration considered here is extracted from validated MLS and based on 100 layers per crystallite.

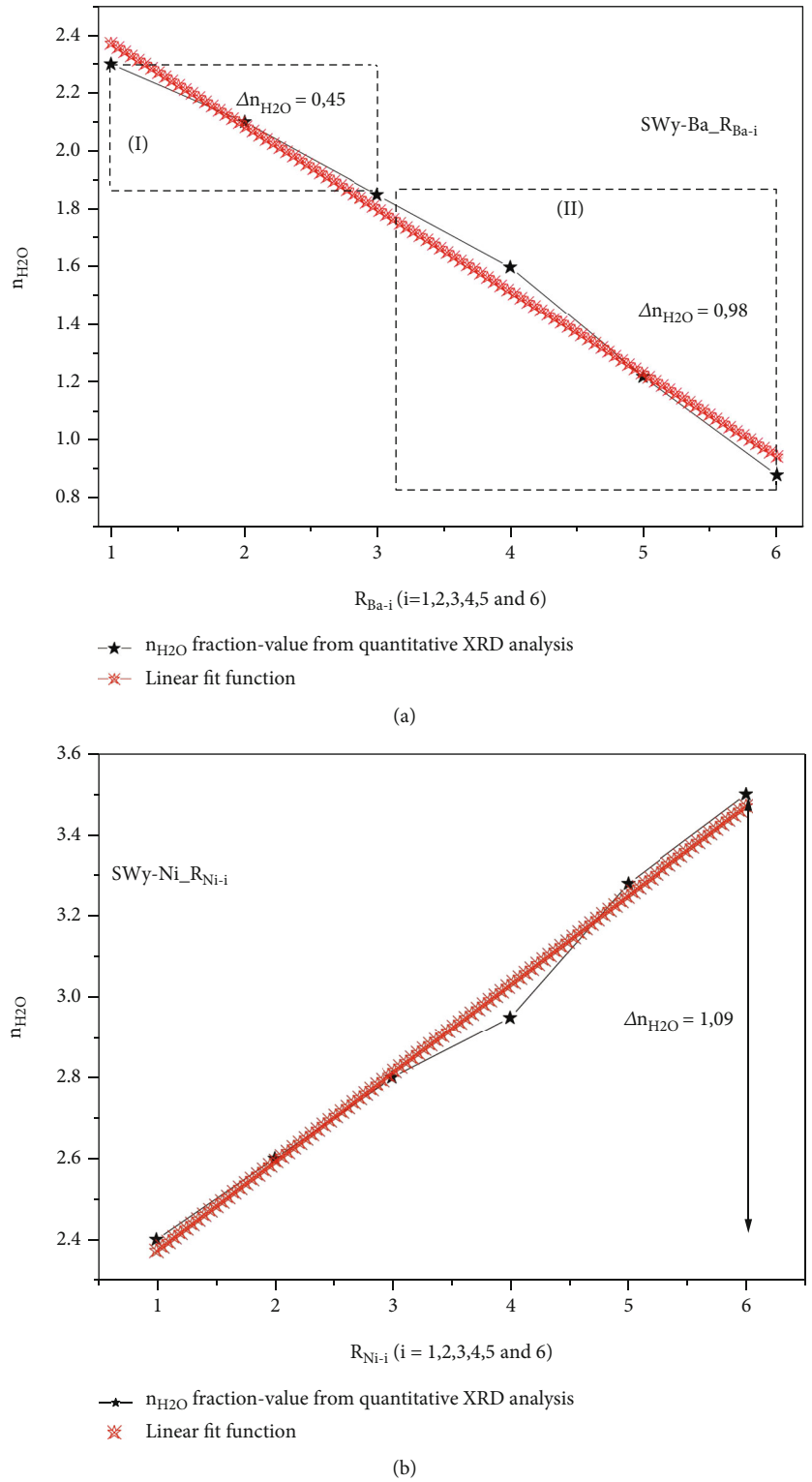

FIGURE 5: n_{H2O} abundance fluctuation versus R_{M-i} values in the case of (a) SWy-Ba and (b) SWy-Ni complexes. Red color: the used linear fit.

process was observed in the case of SWy-Ba samples by varying the surrounding solid/liquid ratio. For SWy-Ni, the cation exchange rises and the starting material response is more understood. Structural changes (such as layer thickness fluctuations, FWHM, ξ parameter, and even more up to the layer stacking mode and the average layer number in the crystallite) and the insight of the mineral CEC running mode are closely related to the discretization of the hydration states. The individual layer type abundance deduced from the optimized theoretical MLS used to reproduce the experimental XRD profiles was presented in Figure 6. For SWy-Ba samples, a minor hydration state

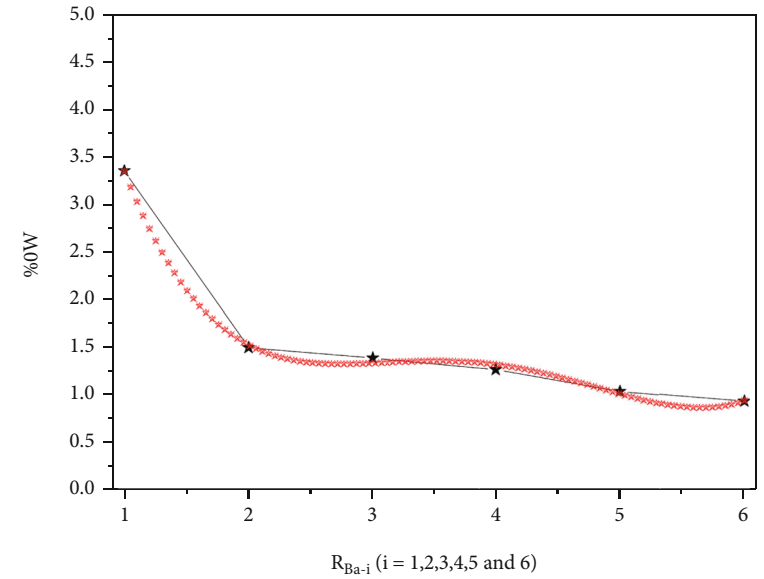

(a)

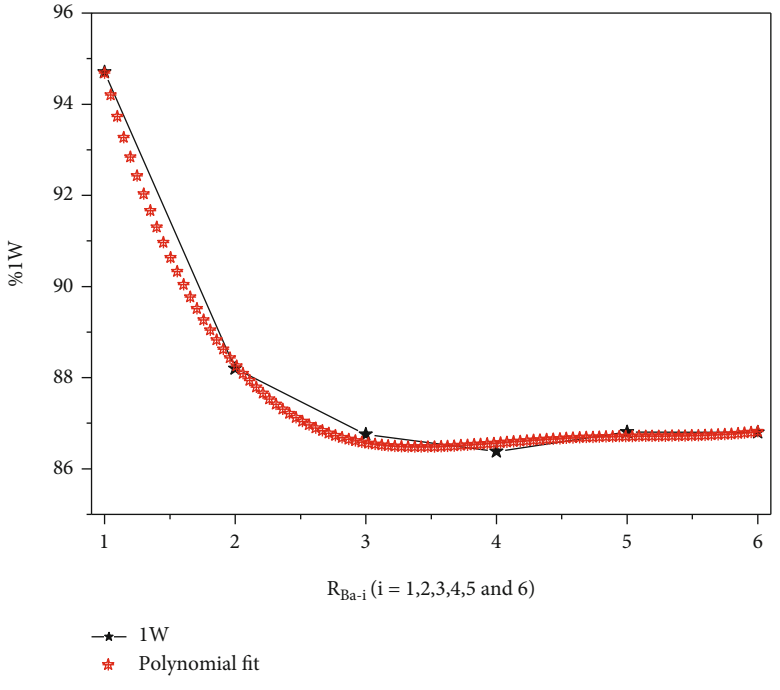

(b)

Figure 6: Continued.

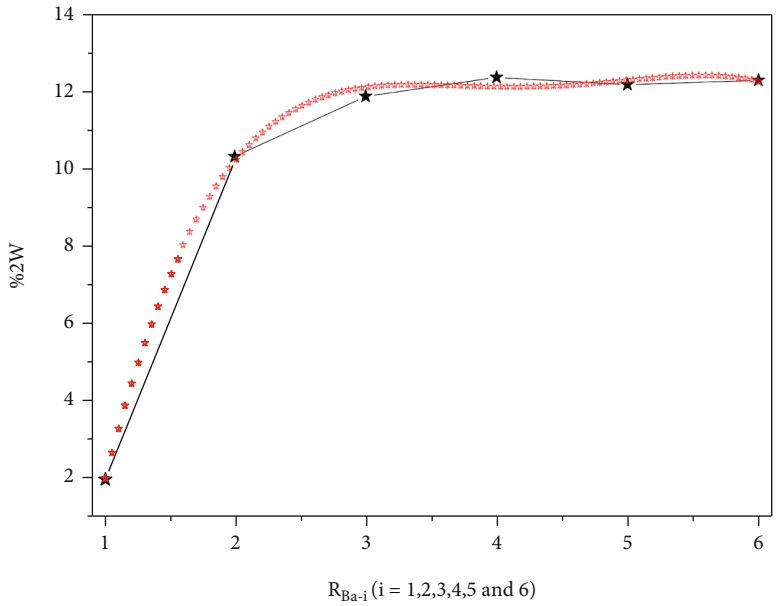

(c)

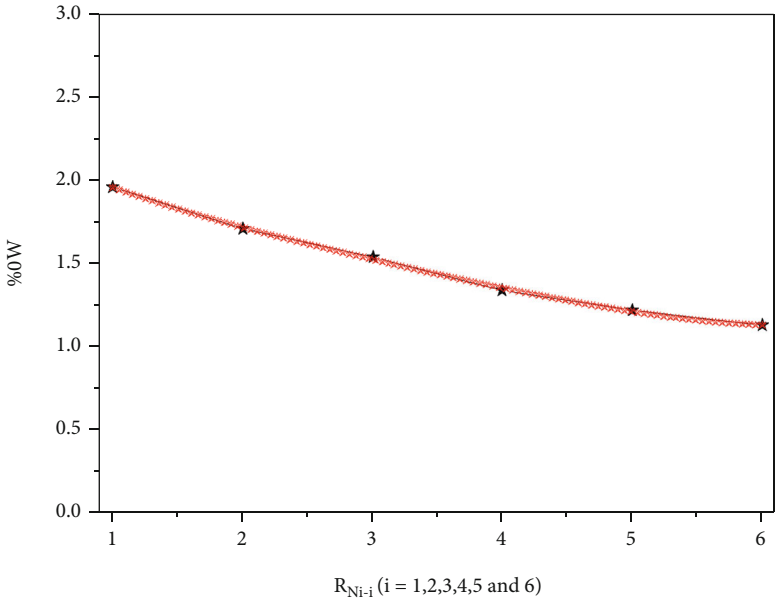

(d)

Figure 6: Continued.

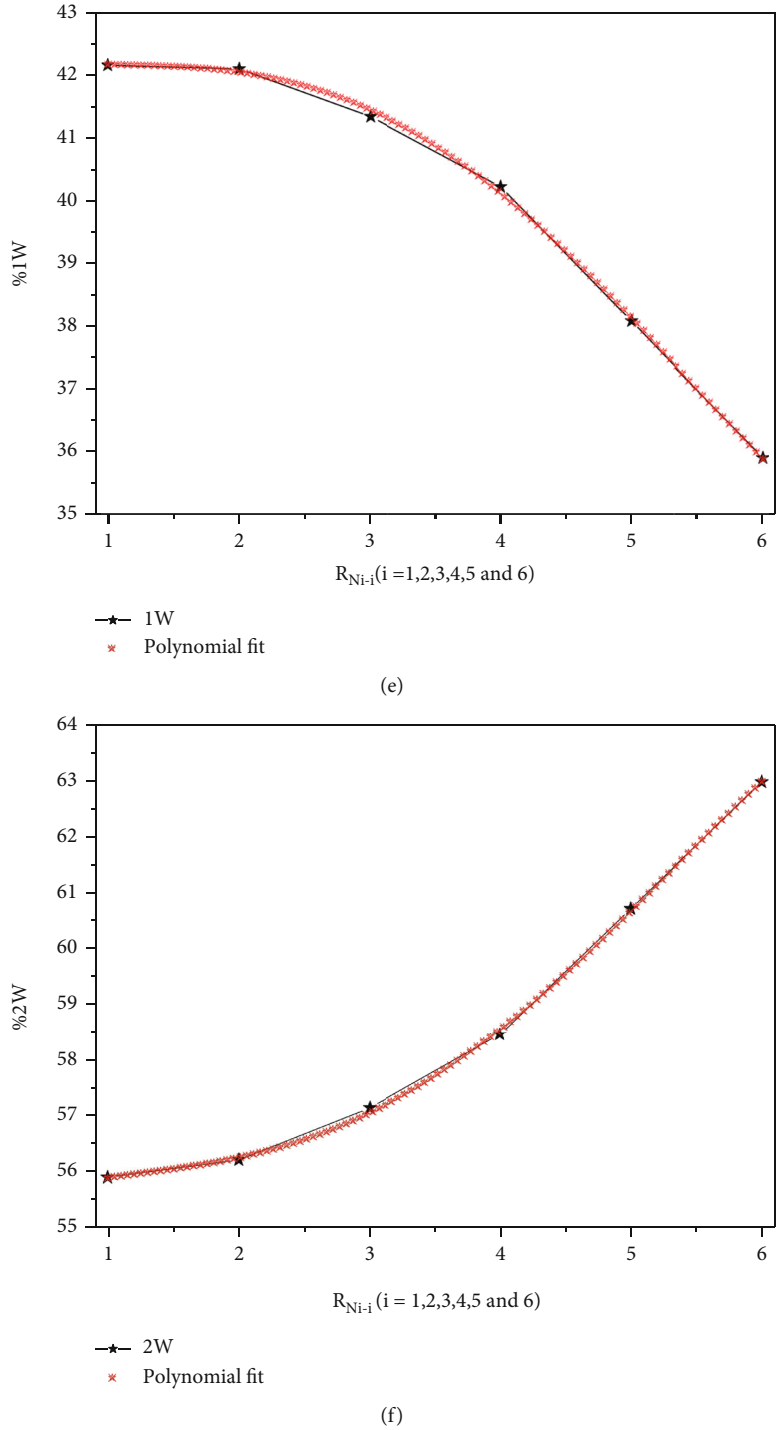

Figure 6: Simulation of $0W$, $1W$, and $2W$ amount evolution versus constraint strength. (a) $0W$_Ba; (b) $1W$_Ba; (c) $2W$_Ba; (d) $0W$_Ni; (e) $1W$_Ni; (f) $2W$_Ni.

fluctuation for the $0W$ and $2W$ (2.4% ($0W$) and 10% ($2W$)) is observed.

This is explained by an almost absence of the cation exchange process, and the starting sample is indifferent to the applied constraint variation despite the exchange equilibrium time provided. Knowing that water phase abundances are normalized to 100%, we find this result in the evolution of the $1W$ hydration state which even though with these fluctuations, the sample remains practically at $1W$ and the IS retains its original identity. This evolution was fitted using a polynomial regression approach in order to characterize the observed fluctuations by an empirical rule (Table 7). We reported in Figure 6 an individually polynomial regression approach which directs

Table 7: Theoretical value deduced from polynomial regression fitting which is used to study the evolution of the layer type abundance.

Layer type	Analytical values	Ba^{2+}	Ni^{2+}
$0W$	A_0	9.2400	2.3033
	A_1	−8.9966	−0.4228
	A_2	3.7154	0.0934
	A_3	−0.6552	−0.0167
	A_4	0.0412	0.0012
	Reduced chi-sqr	0.0069	0.0057
	Adj. R-square	0.9913	0.9942
$1W$	A_0	110.0723	42.3833
	A_1	−21.6798	−0.5287
	A_2	7.2986	0.4779
	A_3	−1.0671	−0.1755
	A_4	0.0575	0.0134
	Reduced chi-sqr	0.0865	0.0272
	Adj. R-square	0.9916	0.9956
$2W$	A_0	−19.3123	55.3133
	A_1	30.6765	0.9515
	A_2	−11.0140	−0.5714
	A_3	1.7224	0.1923
	A_4	−0.0987	−0.0146
	Reduced chi-sqr	0.1423	0.0199
	Adj. R-square	0.9914	0.9974

the progress of the layer abundance, related to all exchangeable cations, along the R_{Ba-i} value. For the SWy-Ni sample, a main increase of the $2W$ phase amounts versus the R_{Ni-i} value is observed. This major fluctuation is accompanied by a slow decrease of $0W$ and $1W$ phases. The evolution of all layer type abundance respects a polynomial regression approach (Figure 6 and Table 7). This result can be interpreted by a cation exchange establishment whatever the value of the constraint in the case of the Ni^{2+} cation is.

The polynomial equation is as follows:

$$y = A_0 + A_1 x + A_2 x^2 + A_3 x^3 + A_4 x^4. \quad (5)$$

3.7. Evolution of the Layer Stacking Mode. In this section, the evolution of the proportions of the different kinds of layers W_i and the layer stacking mode, which is described by a set of junction probabilities (P_{ij}) within the clay particle, is investigated [70, 86]. These succession probabilities depend on the phase's composition and the structure order degree. The order is characterized by the "Reichweit (R)" factor indicating the layer range interactions detailed by [87].

The relationship between the solid/liquid ratio and the layer stacking mode within crystallite in the cases of SWy-Ba and SWy-Ni complexes is reported in Table 7.

For Ba^{2+} exchanged montmorillonite, a domination of the segregated stacking mode is observed (Table 8) indicating that it is no longer a question of interstratification or intracrystallite heterogeneity attributed to the coexistence, within the same crystal, of two or more layer types but a real physical mixture between different layer populations. This reading confirms the low achieved cation exchange degree.

Table 8: Layer stacking mode versus the R_{M-i} value.

R_{M-i}	Phases	Layer stacking mode	Description
R_{Ba-1}	1	R0	Total segregation
	2	$R1_{seg}$	Partial segregation
	3	R0	Total segregation
	4	R0	Total segregation
R_{Ba-2}	1	R0	Total segregation
	2	R1	Partial order
	3	R0	Random order
	4	R0	Total segregation
R_{Ba-3}	1	R0	Total segregation
	2	$R1_{seg}$	Partial segregation
	3	R0	Total segregation
R_{Ba-4}	1	R0	Total segregation
	2	$R1_{seg}$	Partial segregation
	3	R0	Total segregation
R_{Ba-5}	1	R0	Total segregation
	2	R1	Partial order
	3	R0	Total segregation
R_{Ba-6}	1	R0	Total segregation
	2	R0	Random order
	3	R0	Total segregation
R_{Ni-1}	1	R0	Random order
	2	R0	Random order
	3	R0	Total segregation
R_{Ni-2}	1	R0	Random order
	2	$R1_{seg}$	Partial segregation
	3	R0	Total segregation
R_{Ni-3}	1	R0	Random order
	2	R0	Random order
	3	R0	Total segregation
R_{Ni-4}	1	R0	Random order
	2	R1	Partial order
	3	R0	Total segregation
R_{Ni-5}	1	R1	Partial order
	2	R1	Partial order
	3	R0	Total segregation
R_{Ni-6}	1	$R1_{seg}$	Partial segregation
	2	R1	Partial order
	3	R0	Total segregation

Table 9: SA_{BET} (single and multipoint BET) and BJH method average pore diameter.

Sample	SA_{BET} (m^2/g) Single-point BET	SA_{BET} (m^2/g) Multipoint BET	Average nanopore diameter (nm) BJH method
SWy-Na	14.7248	14.9021	3.6987
SWy – Ba_R_{Ba-1}	14.8724	14.7324	3.8012
SWy – Ba_R_{Ba-2}	16.0894	16.3198	3.7581
SWy – Ba_R_{Ba-3}	20.9641	21.7342	3.8937
SWy – Ba_R_{Ba-4}	21.8647	21.4286	4.0214
SWy – Ba_R_{Ba-5}	20.5478	20.8674	4.0152
SWy – Ba_R_{Ba-6}	19.7283	20.1798	3.9864
SWy – Ni_R_{Ni-1}	25.8756	25.9756	4.8679
SWy – Ni_R_{Ni-2}	26.8426	26.9924	4.8721
SWy – Ni_R_{Ni-3}	28.4628	28.9745	4.9334
SWy – Ni_R_{Ni-4}	29.2587	29.8674	5.0158
SWy – Ni_R_{Ni-5}	32.1597	32.4421	4.9901
SWy – Ni_R_{Ni-6}	32.1897	32.2019	4.9860

For Ni^{2+} exchanged montmorillonite, the ordered stacking mode distributions, with its two aspects (e.g., partial and random order, Table 8), are present along the R_{Ni-i} value. Indeed, on the diagram of [67], the partial order is the upper limit of the MPDO maximum order zone with $R = 1$, which is defined by prohibiting the succession of two layers in minority proportion [70]. On the other hand, in the random stacking order, no stacking sequence is prohibited and the probability of a layer appearing in a sequence does not depend on therefore its proportion. This confirms the interstratification within the crystallite which will generate a loss of rationality in the 001 reflections series on the XRD diffractogram.

3.8. BET and BJH Pore Size Distribution Analysis. The stacking of the TOT layers in montmorillonite in the *c* direction is the master variable that determines the specific internal and external surface areas. The montmorillonite layers, and the saturated pores which delineate, control the diffusion properties and the transport of solutes in engineered environments. Indeed, the variation of the solid/liquid ratio affects the colloidal properties of the final clay suspension in addition to these effects on the intrinsic structural properties of the starting materials. Clay is a mineral which occurs at the nanometric scale with a 2D layer structure whose cohesion is ensured by physical interactions [88]. The structural basis of montmorillonite porosity remains poorly characterized due to the difficulty in visualizing hydrated samples in their native state. Here, the BET and BJH pore size distribution analyses are used to decode the possible links and relation between the solid/liquid ratio of the global solution, the CEC, and the size and/or shape of the crystallites. BET is an appropriate method to assess chemical transformation on the external surface of a porous 2D structure, like a clay layer, due to the impermeability of the interlamellar space versus nitrogen. In this work, both single-point and multipoint BET methods were considered to determine the surface area (SA) from nitrogen isotherms [76]. The mean pore diameter for each sample is determined by the BJH method. The BET surface area and the average nanopore diameter regardless of the R_{M-I} value are summarized in Table 9. The obtained results show an increase in the calculated external surface in the case of the Ni exchange specimen compared to the barium-saturated sample. This growth depends on the value of the solid/liquid ratio imposed by the starting solution. The calculated external surface for the SWy-Ni sample increases proportionally with the constraint strength, contrary to that for the SWy-Ba sample, where the sample practically maintains values very close to those of the starting sample which probably indicates minimal IS disturbance. This can be interpreted by the diffusion coefficient change with the preparation and packing density of the montmorillonite and with the concentrations of the major ions [89–95].

Using the BET method and SA measurement (Figure 7), a nitrogen adsorption- (ads-) desorption (des) isotherm has been traced for all studied samples. Indeed, the shapes of the obtained curves can be described by a pore distribution categorized under type II adsorption isotherms in the classification of Brunauer, Deming, Deming, and Teller (BDDT) [75–77]. This classification is attributed to the sample mesoporous texture with large pores (in addition to the nanopores). Indeed, according to an IUPAC definition, porous materials are classified into three major categories depending on their pore sizes: microporous materials with pore sizes below 2 nm, mesoporous materials with pore sizes between 2 and 50 nm, and macroporous materials with pore sizes exceeding 50 nm [96].

Larges pores are partly due to the CEC saturation in the case of Ni^{2+} cation. Given the applied constraint strength (R_{M-i}) and the exchangeable cation nature that this intercalation promotes, the exfoliation process and that thereafter increase the porosity degree. In addition and because of the limited nitrogen capacity to cover only the outer primary

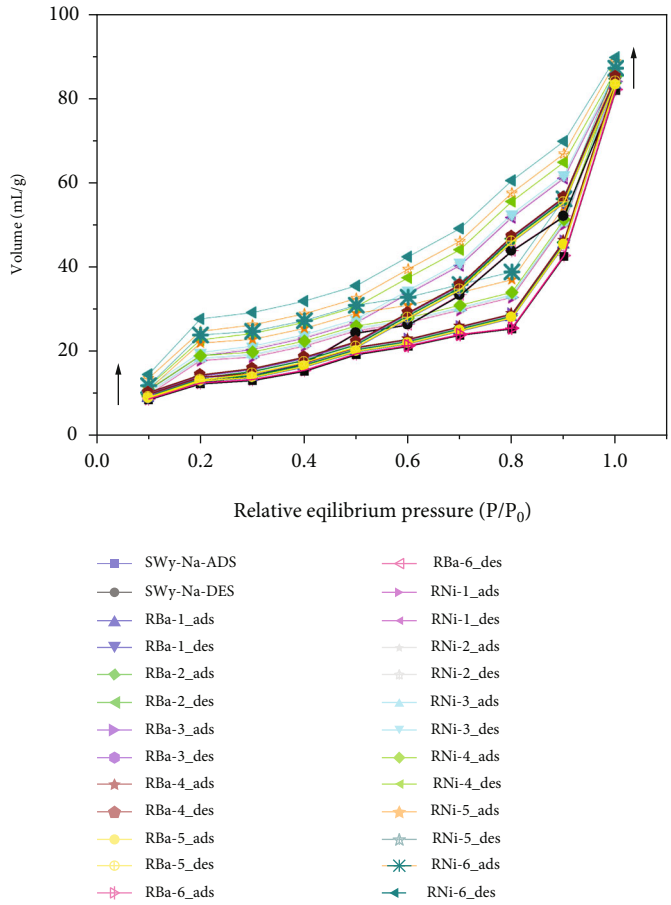

Figure 7: Nitrogen adsorption- (ads-) desorption (des) isotherms.

surface without having access to the interlayer space (IS), an asymptotic approach to the restrictive quantity is observed along the nitrogen isotherms. It should be noted that the surface area concept is unable to give a global description of the texture in the case of 2D porous materials (clay fraction). Indeed, it is essential to differentiate between external, internal, and interlamellar surface areas for clays. For this and for a more quantitative description of the porosity texture, pore size (PS) and pore size distribution (PSD) studies are imposed. The PSD in the mesopore region can be determined by the BJH method assuming several propositions and approximations such as

(i) P_0 and P are the vapor pressure of the bulk liquid nitrogen and the equilibrium pressure of desorption at the liquid nitrogen temperature (~77 K), respectively

(ii) V_{Mi}, V_{Me}, and V_{Ma} (all in mL/g), define the volumes of micropores, mesopores, and macropores including nanopores in one-gram solid

(iii) The specific micromesopore volumes ($V = V_{Mi} + V_{Me}$) are obtained from the desorption data, at the relative equilibrium pressure (P/P_0)

(iv) Cylindrical pores shape (with a radius (r) approximately half of its width)

(v) Cylindrical mesopores (with radii (r) corresponding to v values which were calculated from the corrected Kelvin equation using P/P_0 values)

(vi) Macropores do not affect the adsorptive properties [79]

The $V - r$ (cumulative pore volume vs pore radius) plots and the mesopore PSD are given in Figure 8. An increase in the pore sizes in the case of the Ni^{2+} cation is observed compared to the Ba^{2+} cation.

By intercepting the extrapolations of each PSD curve related to each sample, the V_{Mi} and V_{Me} can be determined. The V_{Me} ranges from 0.045 for R_{Ni-1} to 0.07 for R_{Ni-6} which proves a remarkable increase probably due to the completion of the cation exchange process (Figure 8). The radius derivative of the $V - r$ curve for all samples is given in Figure 9. Indeed, the maximum mesopore volume (0.00674 mL/g) is obtained for the R_{Ni-6} sample. All the determined $V - r$ values, in the case of SWy-Ni, are far greater than those relating to SWy-Ba. For the SWy-Ba sample, the maximum mesopore volume is 0.00351 mL/g and obtained at R_{Ba-2}.

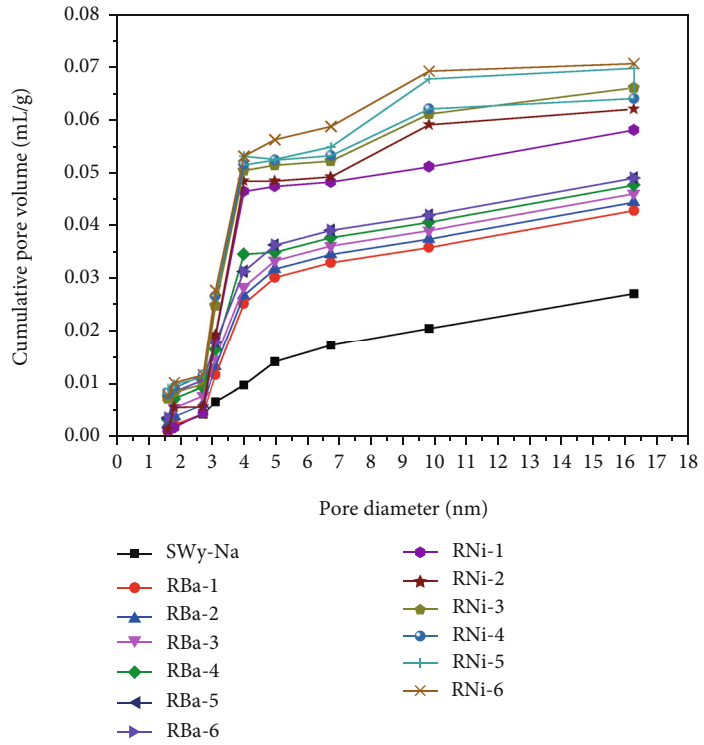

Figure 8: The pore size distribution (PSD) curve for the different studied samples ($V - r$).

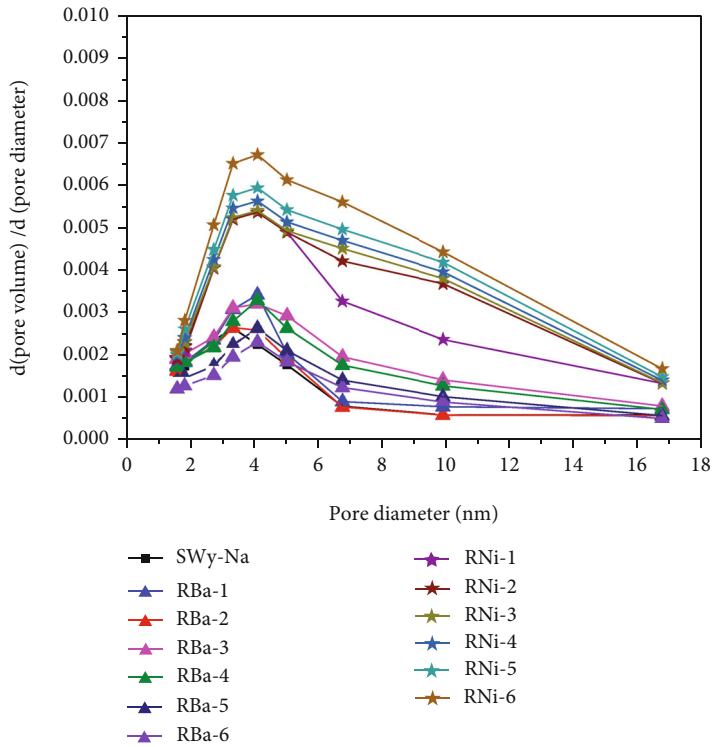

Figure 9: The derivative pore size distribution curve.

This behavior persists up to R_{Ba-4} which is consistent with the quantitative XRD analysis which predicts the cation exchange process beginning at R_{Ba-2}. Commonly, the variation of the solid/liquid ratio affected the volume of the mesopores, which are in any case greater than those determined for the starting sample. For all samples, the mesopore radii

varied between 1.586 and 16.739 nm (Figure 9). In addition and due to the applied constraint and the exchangeable cation nature, a reduction of the microporous distribution in favor of mesoporous distribution is observed. The porosity investigation using the BET-BJH method confirms the obtained results from the XRD modelling approach indicating the quasiachievement of the exchange process regardless of the R_{Ni-i} value, layer exfoliation, and crystallite size fluctuations. This structural response to the hydrological disturbance clearly shows a very specific behavior depending on the constraint strength and the nature of the exchangeable cation.

4. Conclusion

This work focuses on the hydration behavior, the IS perturbation, the CEC fluctuations, and the structural changes of Wyoming montmorillonite according to the geochemical constraints which are created at the laboratory scale (e.g., variable solid/liquid ratio (R_{M-i}) in the case of solution saturated by Ba^{2+} or Ni^{2+}). These goals are achieved by combining the results from the XRD profile modelling approach with the developed mathematical arsenal behind and the adsorption measurement outcomes. Indeed, this theoretical approach allows us to quantify the IS configuration versus applied constraint (e.g., the nature, abundance, size, position, organization of the interlamellar species along the c -axis, and the stacking modes in the crystallites). The modelling approach also allowed us to identify the heterogeneities of structures in the samples studied, to shed light on unknown hydration behavior, and disclosed the influence of macroscopic constraints on the microscopic hydration properties. The obtained results, at room temperature and without any applied constraint, show that the starting SWy-Na complex exhibits a homogeneous $1W$ hydration state and the SWy-Ba and SWy-Ni complexes a homogeneous $2W$ hydration state, which is in accordance with the previous work of [26, 38, 54]. The qualitative XRD investigation of the R_{M-i} variation effect on CEC properties shows an interstratified hydration character for all complexes probably attributed to the incomplete or partial cation exchange process. The quantitative XRD analysis shows in the case of Ba^{2+} cation that

(i) Whatever the constraint strength, the sample exhibits a heterogeneous hydration behavior traduced by the coexistence of $0W$, $1W$, and $2W$ hydration states within the crystallite

(ii) The theoretical decomposition of the experimental XRD profiles allowed us to identify all existing different layer populations and their stacking mode

(iii) A domination of the segregated stacking mode versus the R_{Ba-i} value indicating the formation of a real physical mixture between different layer populations

The quantitative investigation of the effect of the variation of the solid/liquid ratio in the case of the Ni^{2+} cation shows that

(i) An interstratification was approved by the coexistence of the three hydration states (i.e., $0W$, $1W$, and $2W$) whatever the R_{Ni-i} value is

(ii) There is coexistence within the crystallite of different kinds of layer populations stacked according to a specific set of junction probabilities

(iii) For low R_{Ni-i} values, the appearance of intrinsic layer hydration heterogeneity with variable filling of the IS confirms the partial cation exchange process

In addition, the XRD modelling approach allowed us to assign a hydration footprint response and to map the interstratification of the different populations of layers, for each R_{M-i} value. The adsorption measurement results based on BET and BJH pore size distribution analyses confirm the exfoliation process versus applied constraint. Indeed, the mesopore $V - r$ shows elevated values in the case of Ni^{2+} cation indicating new IS configuration at the layer scale and a size decrease at the crystallite scale.

Data Availability

No data were used to support this study.

Disclosure

The results presented are a part of the Ph.D. thesis of Chadha Mejri (CM) realized at LR19ES20: Ressources, Matériaux et Ecosystèmes (RME), Faculty of Sciences of Bizerte, University of Carthage, 7021 Zarzouna, Tunisia and supervised by Dr. Walid Oueslati (WO).

Conflicts of Interest

The authors declare no conflict of interest.

Authors' Contributions

Dr. Walid Oueslati (WO) supervised the study, contributed in the experimental result acquisition, XRD profiles modeling approach, the paper writing and the proof reading of the manuscript.

Acknowledgments

CM acknowledges WO for the original idea of the work, the fruitful discussions about the XRD modelling approach, and the montmorillonite hydration behavior.

References

[1] T. Al-Ani and O. Sarapaa, "Clay and clay mineralogy: physical-chemical properties and industrial uses," *Geological Survey of Finland*, vol. 1, pp. 3-4, 2008.

[2] S. Dultz, J. H. An, and B. Riebe, "Organic cation exchanged montmorillonite and vermiculite as adsorbents for Cr(VI): effect of layer charge on adsorption properties," *Applied Clay Science*, vol. 67-68, pp. 125–133, 2012.

[3] X. Gu, L. J. Evans, and S. J. Barabash, "Modeling the adsorption of Cd (II), Cu (II), Ni (II), Pb (II) and Zn (II) onto montmorillonite," *Geochimica et Cosmochimica Acta*, vol. 74, no. 20, pp. 5718–5728, 2010.

[4] A. E. Burakov, E. V. Galunin, I. V. Burakova et al., "Adsorption of heavy metals on conventional and nanostructured materials for wastewater treatment purposes: a review," *Ecotoxicology and Environmental Safety*, vol. 148, pp. 702–712, 2018.

[5] P. Jacquier, D. Hainos, J. C. Robinet et al., "The influence of mineral variability of Callovo-Oxfordian clay rocks on radionuclide transfer properties," *Applied Clay Science*, vol. 83-84, pp. 129–136, 2013.

[6] F. Dolder, U. Mäder, A. Jenni, and B. Münch, "Alteration of MX-80 bentonite backfill material by high-pH cementitious fluids under lithostatic conditions–an experimental approach using core infiltration techniques," *Geological Society, London, Special Publications*, vol. 443, no. 1, pp. 281–305, 2017.

[7] K. Kolomá and R. Červinka, "Study of 85Sr transport through a column filled with crushed granite in the presence of bentonite colloids," *Geological Society, London, Special Publications*, vol. 443, no. 1, pp. 193–203, 2017.

[8] X. Su, S. Nguyen, E. Haghighat et al., "Characterizing the mechanical behaviour of the Tournemire argillite," *Geological Society, London, Special Publications*, vol. 443, no. 1, pp. 97–113, 2017.

[9] M. Ballini, C. Chautard, J. Nos et al., "A multi-scalar study of the long-term reactivity of uranium mill tailings from Bellezane site (France)," *Journal of Environmental Radioactivity*, vol. 218, pp. 106223–106223, 2020.

[10] W. Hu, S. Lu, W. Song et al., "Competitive adsorption of U(VI) and Co(II) on montmorillonite: a batch and spectroscopic approach," *Applied Clay Science*, vol. 157, pp. 121–129, 2018.

[11] D. Deneele, O. Cuisinier, V. Hallaire, and F. Masrouri, "Microstructural evolution and physico-chemical behavior of compacted clayey soil submitted to an alkaline plume," *Journal of Rock Mechanics and Geotechnical Engineering*, vol. 2, no. 2, pp. 169–177, 2010.

[12] W. Oueslati, H. B. Rhaiem, and A. B. H. Amara, "XRD investigations of hydrated homoionic montmorillonite saturated by several heavy metal cations," *Desalination*, vol. 271, no. 1-3, pp. 139–149, 2011.

[13] D. A. Glatstein and F. M. Francisca, "Influence of pH and ionic strength on Cd, Cu and Pb removal from water by adsorption in Na-bentonite," *Applied Clay Science*, vol. 118, pp. 61–67, 2015.

[14] S. Yingying, Z. Baoqiang, and W. Yang, "Application of clay minerals in remediation of heavy metal pollution in soil," *E3S Web of Conferences*, vol. 204, p. 01011, 2020.

[15] B. O. Otunola and O. O. Ololade, "A review on the application of clay minerals as heavy metal adsorbents for remediation purposes," *Environmental Technology & Innovation*, vol. 18, p. 100692, 2020.

[16] S. Gu, X. Kang, L. Wang, E. Lichtfouse, and C. Wang, "Clay mineral adsorbents for heavy metal removal from wastewater: a review," *Environmental Chemistry Letters*, vol. 17, no. 2, pp. 629–654, 2019.

[17] D. Borden and R. F. Giese, "Baseline studies of the clay minerals society source clays: cation exchange capacity measurements by the ammonia-electrode method," *Clays Clay Miner.*, vol. 49, no. 5, pp. 444-445, 2001.

[18] A. U. Dogan, M. Dogan, M. Onal, Y. Sarikaya, A. Aburub, and D. E. Wurster, "Baseline studies of the clay minerals society source clays: specific surface area by the Brunauer Emmett Teller (BET) method," *Clays and Clay Minerals*, vol. 54, no. 1, pp. 62–66, 2006.

[19] T. Al-Ani and O. Sarapää, "Clay and Clay Mineralogy," *Physical-chemical properties and industrial uses*, 2008.

[20] H. Yin and J. Zhu, "In situ remediation of metal contaminated lake sediment using naturally occurring, calcium-rich clay mineral-based low-cost amendment," *Chemical Engineering Journal*, vol. 285, pp. 112–120, 2016.

[21] D. Mohapatra, D. Mishra, G. R. Chaudhury, and R. P. Das, "Arsenic adsorption mechanism on clay minerals and its dependence on temperature," *Korean Journal of Chemical Engineering*, vol. 24, no. 3, pp. 426–430, 2007.

[22] H. Es-sahbany, M. Berradi, S. Nkhili et al., "Removal of heavy metals (nickel) contained in wastewater-models by the adsorption technique on natural clay," *Materials Today: Proceedings*, vol. 13, pp. 866–875, 2019.

[23] C. Coles and R. Yong, "Aspects of kaolinite characterization and retention of Pb and Cd," *Applied Clay Science*, vol. 22, no. 1–2, pp. 39–45, 2002.

[24] G. J. Churchman, W. P. Gates, B. K. G. Theng, and G. Yuan, "Chapter 11.1 Clays and Clay Minerals for Pollution Control," *Dev. Clay Sci.*, vol. 1, pp. 625–675, 2006.

[25] J. H. Potgieter, S. S. Potgieter-Vermaak, and P. D. Kalibantonga, "Heavy metals removal from solution by palygorskite clay," *Minerals Engineering*, vol. 19, no. 5, pp. 463–470, 2006.

[26] R. Chalghaf, W. Oueslati, M. Ammar, H. B. Rhaiem, and A. B. H. Amara, "Effect of temperature and pH value on cation exchange performance of a natural clay for selective (Cu2+, Co2+) removal: equilibrium, sorption and kinetics," *Progress in Natural Science: Materials International*, vol. 23, no. 1, pp. 23–35, 2013.

[27] A. R. A. Usman, Y. Kuzyakov, and K. Stahr, "Effect of clay minerals on extractability of heavy metals and sewage sludge mineralization in soil," *Chemistry and Ecology*, vol. 20, no. 2, pp. 123–135, 2004.

[28] G. Zhang, Y. Lin, and M. Wang, "Remediation of copper polluted red soils with clay materials," *Journal of Environmental Sciences*, vol. 23, no. 3, pp. 461–467, 2011.

[29] M. M. Wahba, B. F. Labib, K. H. M. Darwish, and M. A. Zaghloul, "Application of some clay minerals to eliminate the hazards of heavy metals in contaminated soils," in *15th International Conference on Environmental Science and Technology, CEST*, Rhodes, Greece, 2017.

[30] V. Chantawong, N. W. Harvey, and V. N. Bashkin, "Comparison of heavy metal adsorptions by Thai kaolin and ballclay," *Water, Air, and Soil Pollution*, vol. 148, no. 1/4, pp. 111–125, 2003.

[31] A. Alshameri, H. He, C. Xin et al., "Understanding the role of natural clay minerals as effective adsorbents and alternative source of rare earth elements: adsorption operative parameters," *Hydrometallurgy*, vol. 185, pp. 149–161, 2019.

[32] D. M. Manohar, K. Anoop Krishnan, and T. S. Anirudhan, "Removal of mercury(II) from aqueous solutions and chloralkali industry wastewater using 2-mercaptobenzimidazole-clay," *Water Research*, vol. 36, no. 6, pp. 1609–1619, 2002.

[33] W. Zhang, Y. An, S. Li et al., "Enhanced heavy metal removal from an aqueous environment using an eco-friendly and sustainable adsorbent," *Science Reports*, vol. 10, article 16453, 2020.

[34] G. W. Brindley and G. Brown, *Crystal Structures of Clay Minerals and Their X Ray Identification, Monograph 5*, Mineralogical Society, London, UK, 1980.

[35] A. C. D. Newman, "Chemistry of clays and clay minerals," *Mineral Society Monograph, London*, vol. 6, p. 480, 1987.

[36] N. Güven, "Hydrous phyllosilicates (exclusive of micas)," *Reviews in Mineralogy*, S. W. Bailey, Ed., vol. 19, p. 497, 1988.

[37] T. Sato, T. Watanabe, and R. Otsuka, "Effects of layer charge, charge location, and energy change on expansion properties of dioctahedral smectites," *Clays and Clay Minerals*, vol. 40, no. 1, pp. 103–113, 1992.

[38] I. Bérend, J. M. Cases, M. François et al., "Mechanism of adsorption and desorption of water Vapor by homoionic montmorillonites: 2. The Li+, Na+, K+, Rb+, and Cs +-Exchanged forms," *Clays and Clay Minerals*, vol. 43, no. 3, pp. 324–336, 1995.

[39] J. M. Cases, I. Bérend, M. François, J. P. Uriot, L. J. Michot, and F. Thomas, "Mechanism of adsorption and desorption of water Vapor by homoionic montmorillonite: 3. The Mg2+, Ca2+, Sr2+ and Ba2+ exchanged forms," *Clays and Clay Minerals*, vol. 45, no. 1, pp. 8–22, 1997.

[40] W. Oueslati, H. Ben Rhaiem, and A. Ben Haj Amara, "Effect of relative humidity constraint on the metal exchanged montmorillonite performance: An XRD profile modeling approach," *Applied Surface Science*, vol. 261, pp. 396–404, 2012.

[41] K. Yotsuji, Y. Tachi, H. Sakuma, and K. Kawamura, "Effect of interlayer cations on montmorillonite swelling: comparison between molecular dynamic simulations and experiments," *Applied Clay Science*, vol. 204, p. 106034, 2021.

[42] G. Wang, L. Ran, J. Xu et al., "Technical development of characterization methods provides insights into clay mineral-water interactions: a comprehensive review," *Applied Clay Science*, vol. 206, p. 106088, 2021.

[43] A. Asaad, F. Hubert, E. Ferrage et al., "Role of interlayer porosity and particle organization in the diffusion of water in swelling clays," *Applied Clay Science*, vol. 207, p. 106089, 2021.

[44] M. V. Villar and A. Lloret, "Influence of temperature on the hydro-mechanical behaviour of a compacted bentonite," *Applied Clay Science*, vol. 26, no. 1-4, pp. 337–350, 2004.

[45] R. Chalghaf, W. Oueslati, M. Ammar, H. B. Rhaiem, and A. B. H. Amara, "Effect of an "in situ" hydrous strain on the ionic exchange process of dioctahedral smectite: Case of solution containing (Cu^{2+}, Co^{2+}) cations," *Applied Surface Science*, vol. 258, no. 22, pp. 9032–9040, 2012.

[46] M. Ammar, W. Oueslati, N. Chorfi, and H. Ben Rhaiem, "Interlamellar space configuration under variable environmental conditions in the case of Ni-exchanged montmorillonite: quantitative XRD analysis," *Journal of Nanomaterials*, vol. 2014, Article ID 284612, 13 pages, 2014.

[47] K. K. Norrfors, M. Bouby, S. Heck et al., "Montmorillonite colloids: I. Characterization and stability of dispersions with different size fractions," *Applied Clay Science*, vol. 114, pp. 179–189, 2015.

[48] R. A. Schoonheydt and C. T. Johnston, "The surface properties of clay minerals," *EMU Notes Mineral*, vol. 11, pp. 337–373, 2011.

[49] A. S. Anastácio, A. Aouad, P. Sellin, J. D. Fabris, F. Bergaya, and J. W. Stucki, "Characterization of a redox-modified clay mineral with respect to its suitability as a barrier in radioactive waste confinement," *Applied Clay Science*, vol. 39, no. 3–4, pp. 172–179, 2008.

[50] P. Sellin and O. X. Leupin, "The use of clay as an engineered barrier in radioactive-waste management–a review," *Clays and Clay Minerals*, vol. 61, no. 6, pp. 477–498, 2013.

[51] V. V. Krupskaya, S. V. Zakusin, E. A. Tyupina, O. V. Dorzhieva, M. S. Chernov, and Y. V. Bychkova, "Transformation of structure and adsorption properties of montmorillonite under thermochemical treatment," *Geochemistry International*, vol. 57, no. 3, pp. 314–330, 2019.

[52] N. P. Laverov, S. V. Yudintsev, B. T. Kochkin, and V. I. Malkovsky, "The Russian strategy of using crystalline rock as a repository for nuclear waste," *Elements*, vol. 12, no. 4, pp. 253–256, 2016.

[53] R. Pusch, S. Knutsson, L. al-Taie, and M. H. Mohammed, "Optimal ways of disposal of highly radioactive waste," *Natural Science*, vol. 4, no. 11, pp. 906–918, 2012.

[54] F. M. Huber, S. Heck, L. Truche et al., "Radionuclide desorption kinetics on synthetic Zn/Ni-labeled montmorillonite nanoparticles," *Geochimica et Cosmochimica Acta*, vol. 148, pp. 426–441, 2015.

[55] M. Birgersson and O. Karnland, "Ion equilibrium between montmorillonite interlayer space and an external solution–Consequences for diffusional transport," *Geochimica et Cosmochimica Acta*, vol. 73, no. 7, pp. 1908–1923, 2009.

[56] C. A. J. Appelo, L. R. van Loon, and P. Wersin, "Multicomponent diffusion of a suite of tracers (HTO, Cl, Br, I, Na, Sr, Cs) in a single sample of Opalinus Clay," *Geochimica et Cosmochimica Acta*, vol. 74, no. 4, pp. 1201–1219, 2010.

[57] A. Rybalchenko, M. Pimenov, and P. Kostin, "Injection disposal of hazardous and industrial wastes, scientific and engineering aspects," in *Deep Injection Disposal of Liquid Radioactive Waste in Russia*, Academic Press, New York, 1998.

[58] W. Oueslati, M. Ammar, and N. Chorfi, "Quantitative XRD analysis of the structural changes of Ba-exchanged montmorillonite: effect of an in situ hydrous perturbation," *Minerals*, vol. 5, no. 3, pp. 507–526, 2015.

[59] W. F. Moll, "Baseline studies of the Clay Minerals Society source clays: geological origin," *Clays and Clay Minerals*, vol. 49, no. 5, pp. 374–380, 2001.

[60] A. R. Mermut and A. F. Cano, "Baseline studies of the Clay Minerals Society source clays: chemical analyses of major elements," *Clays and Clay Minerals*, vol. 49, no. 5, pp. 381–386, 2001.

[61] M. Ammar, W. Oueslati, H. Ben Rhaiem, and A. Ben Haj Amara, "Quantitative XRD analysis of the dehydration–hydration performance of (Na+, Cs+) exchanged smectite," *Desalination and Water Treatment*, vol. 52, no. 22–24, pp. 4314–4333, 2014.

[62] S. H. Lin and R. S. Juang, "Heavy metal removal from water by sorption using surfactant-modified montmorillonite," *Journal of Hazardous Materials B*, vol. 92, no. 3, pp. 315–326, 2002.

[63] K. G. Bhattacharyya and S. S. Gupta, "Adsorption of a few heavy metals on natural and modified kaolinite and montmorillonite: A review," *Advances in Colloid and Interface Science*, vol. 140, no. 2, pp. 114–131, 2008.

[64] K. G. Bhattacharyya and S. S. Gupta, "Adsorption of Co(II) from aqueous medium on natural and acid activated Kaolinite and montmorillonite," *Separation Science and Technology*, vol. 42, no. 15, pp. 3391–3418, 2007.

[65] K. S. Abou-el-Sherbini and M. M. Hassanien, "Study of organically-modified montmorillonite clay for the removal of

copper(II)," *Journal of Hazardous Materials*, vol. 184, no. 1-3, pp. 654–661, 2010.

[66] G. W. Brindley, T. Suzuki, and M. Thiry, "Interstratified kaolinite/smectites from the Paris Basin ; correlations of layers proportions, chemical compositions and other data," *Bulletin de Minéralogie*, vol. 106, no. 4, pp. 403–410, 1983.

[67] D. M. Moore and R. C. Reynolds Jr., *X-ray diffraction and the identification and analysis of clay minerals*, Oxford University Press (OUP), 1989.

[68] G. Lagaly and S. Ziesmer, "Colloid chemistry of clay minerals: the coagulation of montmorillonite dispersions," *Advances in Colloid and Interface Science*, vol. 100-102, pp. 105–128, 2003.

[69] S. W. Bailey, "Nomenclature for regular interstratifications," *American Mineralogist*, vol. 67, pp. 394–398, 1982.

[70] V. A. Drits and C. Tchoubar, *X-Ray Diffraction by Disordered Lamellar Structures: Theory and Application to Microdivided Silicates and Carbons*, Springer Verlag, New York, 1990.

[71] B. A. Sakharov and B. Lanson, "X-ray identification of mixedlayer structures. Modelling of diffraction effects," in *Handbook of Clay Science*, F. Bergaya and G. Lagaly, Eds., vol. 5B, pp. 51–135, Elsevier, Amsterdam, Netherlands, 2013.

[72] E. Ferrage, B. Lanson, B. A. Sakharov, and V. A. Drits, "Investigation of smectite hydration properties by modeling experimental X-ray diffraction patterns: Part I. Montmorillonite hydration properties," *American Mineralogist*, vol. 90, no. 8-9, pp. 1358–1374, 2005.

[73] W. Oueslati and M. Meftah, "Discretization of the Water Uptake Process of Na-Montmorillonite Undergoing Atmospheric Stress: XRD Modeling Approach," *Advances in Materials Science and Engineering*, vol. 2018, Article ID 5219624, 17 pages, 2018.

[74] M. Benzina and A. Bellagi, "Détermination des propriétés du réseau poreux de matériau argileux par les techniques d'adsorption d'azote et de porosimétrie au mercure en vue de leur utilisation pour la récupération des gaz," *Annales de Chimie de France*, vol. 15, pp. 315–335, 1990, https://www.scopus.com/inward/record.url?eid=2-s2.0-0007101141&partnerID=10&rel=R3.0.0.

[75] S. Gregg and K. Sing, *Adsorption, Surface Area and Porosity, Second Ed*, Academic Press, London, 1982.

[76] J. Groen, L. A. A. Peffer, and J. Pérez-Ramírez, "Pore size determination in modified micro- and mesoporous materials. Pitfalls and limitations in gas adsorption data analysis," *Microporous and Mesoporous Materials*, vol. 60, no. 1-3, pp. 1–17, 2003.

[77] E. P. Barrett, L. G. Joyner, and P. P. Halenda, "The determination of pore volume and area distributions in porous substances. I. computations from nitrogen isotherms," *Journal of the American Chemical Society*, vol. 73, no. 1, pp. 373–380, 1951.

[78] P. Kumar, R. V. Jasra, and T. S. G. Bhat, "Evolution of porosity and surface acidity in montmorillonite clay on acid activation," *Industrial & Engineering Chemistry Research*, vol. 34, no. 4, pp. 1440–1448, 1995.

[79] F. Rouqueral, J. Rouqueral, and K. Sing, *Adsorption by Powder and Porous Solids*, Academic Press, London, 1999.

[80] W. Oueslati, "Effect of soil solution pH during the tetracycline intercalation on the structural properties of a dioctahedral smectite: microstructural analysis," *Journal of Nanomaterials*, vol. 2019, Article ID 7414039, 17 pages, 2019.

[81] P. Komadel, J. Bujdák, J. Madejová, V. Šucha, and F. Elsass, "Effect of non-swelling layers on the dissolution of reduced-charge montmorillonite in hydrochloric acid," *Clay Minerals*, vol. 31, no. 3, pp. 333–345, 1996.

[82] T. Kozaki, T. Sawaguchi, A. Fujishima, and S. Sato, "Effect of exchangeable cations on apparent diffusion of Ca^{2+} ions in Na- and Ca-montmorillonite mixtures," *Physics and Chemistry of the Earth, Parts A/B/C*, vol. 35, no. 6–8, pp. 254–258, 2010.

[83] S. Babel and T. A. Kurniawan, "Low-cost adsorbents for heavy metals uptake from contaminated water: a review," *Journal of Hazardous Materials B*, vol. 97, no. 1–3, pp. 219–243, 2003.

[84] F. Bergaya and G. Lagaly, "Chapter 1 General Introduction: Clays, Clay Minerals, and Clay Science," *Developments in Clay Science*, vol. 1, pp. 1–18, 2006.

[85] R. D. Shannon, "Revised effective ionic radii and systematic studies of interatomic distances in halides and chalcogenides," *Acta Cryst*, vol. 32, no. 5, pp. 751–767, 1976.

[86] B. Lanson, "Modelling of X-ray diffraction profiles," *EMU Notes in Mineralogy*, vol. 11, pp. 151–202, 2011.

[87] C. M. Bethke, N. Vergo, and S. P. Altaner, "Pathways of smectite illitization," *Clays and Clay Minerals*, vol. 34, no. 2, pp. 125–135, 1986.

[88] M. Auta and B. H. Hameed, "Modified mesoporous clay adsorbent for adsorption isotherm and kinetics of methylene blue," *Chemical Engineering Journal*, vol. 198-199, pp. 219–227, 2012.

[89] J. M. Soler, C. I. Steefel, T. Gimmi, O. X. Leupin, and V. Cloet, "Modeling the ionic strength effect on diffusion in clay. The DR-A experiment at Mont Terri," *ACS Earth and Space Chemistry*, vol. 3, no. 3, pp. 442–451, 2019.

[90] Y. Yang and M. Wang, "Cation diffusion in compacted clay: a pore-scale view," *Environmental Science & Technology*, vol. 53, no. 4, pp. 1976–1984, 2019.

[91] E. Tertre, S. Savoye, F. Hubert, D. Prêt, T. Dabat, and E. Ferrage, "Diffusion of water through the dual-porosity swelling clay mineral vermiculite," *Environmental Science & Technology*, vol. 52, no. 4, pp. 1899–1907, 2018.

[92] Y. W. Hsiao and M. Hedström, "Swelling pressure in systems with Na-montmorillonite and neutral surfaces: a molecular dynamics study," *The Journal of Physical Chemistry C*, vol. 121, no. 47, pp. 26414–26423, 2017.

[93] X. Li, H. Li, and G. Yang, "Configuration, anion-specific effects, diffusion, and impact on counterions for adsorption of salt anions at the interfaces of clay minerals," *The Journal of Physical Chemistry C*, vol. 120, no. 27, pp. 14621–14630, 2016.

[94] Y.-W. Hsiao and M. Hedström, "Molecular dynamics simulations of NaCl permeation in bihydrated montmorillonite interlayer nanopores," *The Journal of Physical Chemistry C*, vol. 119, no. 30, pp. 17352–17361, 2015.

[95] M. A. Glaus, M. Birgersson, O. Karnland, and L. R. van Loon, "Seeming steady-state uphill diffusion of 22Na+ in compacted montmorillonite," *Environmental Science & Technology*, vol. 47, no. 20, pp. 11522–11527, 2013.

[96] K. Ariga, A. Vinu, Y. Yamauchi, Q. Ji, and J. P. Hill, "Nanoarchitectonics for mesoporous materials," *Bulletin of the Chemical Society of Japan*, vol. 85, no. 1, pp. 1–32, 2012.